MANGANESE AND VANADIUM IMPREGNATED ANODE SYSTEMS FOR INTERMEDIATE TEMPERATURE SOLID OXIDE FUEL CELLS

by

Benazir Fazlıoğlu

B.S., Chemistry, Boğaziçi University, 2015

Submitted to the Institute for Graduate Studies in
Science and Engineering in partial fulfillment of
the requirements for the degree of
Master of Science

Graduate Program in Chemistry

Boğaziçi University

2018

Dedicated to my beloved family

ACKNOWLEDGEMENTS

Even though the following thesis is an individual work, it would never have been attainable for me to bring it to a completion without the support, guidance, effort and help of so many people. First of all, it is my deepest sense of gratitude to my thesis advisor Assist. Prof. Oktay Demircan who instilled me with the virtual qualities of being a genuine scientist and chemist. His enthusiasm, intelligence, and patience motivated and strengthened me in every phase of this master project. With his advice and counseling, it became much easier to solve the problems when the going got tough. Besides, he also trained me not to give in immediately when I am alone, to ask the questions in the correct way to myself first and to look at them not only from one side but also from different angles to be able to make my own and truest way. Above all, it is him who taught me to perceive good or bad every conclusion as gain.

I would like to acknowledge and thank my thesis committee members Prof. Amitav Sanyal and Assist. Prof. Aligül Büyükaksoy.

I am thankful to get the chance to have such good friends who shared my highs and lows in the lab. Firstly, I would like to thank Ayşenur Eslem Kısa since she always gave a hand during the stages I am going through in the lab and considered every trouble I had as hers. Furkan Işık and Kıvanç Sağlık deserve thanks for their gentle support and bringing joy to the lab in which I will never forget the days we had together. My thanks also go out to Şule Nihal Öz and Refia Tığrak with whom I enjoyed a very warm form of friendship and never skipped a social activity inside and outside the school even in the busiest days of my research.

I wish to acknowledge the financial support by TUBITAK under the grant number of 214Z094 and Boğaziçi University Research and Development Center for XRD, XPS and SEM analyses. I would also like to gratefully thank all of my teachers and other friends in Department of Chemistry at Boğaziçi University.

Finally, this journey would not have been possible without endless love and support of my beloved family. My heartfelt gratitude goes out to my mother Şemside Fazlıoğlu, my father İsmet Fazlıoğlu, my little sister Berna Fazlıoğlu and my uncle Dr. Mithat Fazlıoğlu. I feel fortunate enough to have such a lovely family. Thank you ever so much for encouraging me to follow my dreams and inspiring me in all of my pursuits.

ABSTRACT

MANGANESE AND VANADIUM IMPREGNATED ANODE SYSTEMS FOR INTERMEDIATE TEMPERATURE SOLID OXIDE FUEL CELLS

Solid Oxide Fuel Cells (SOFC) are environmentally friendly electrochemical energy producing devices that convert chemical energy into electrical energy by oxidizing a fuel. Exhibiting high efficiency in converting fuel to electricity and the tolerance to wide variety of fuels make them promising devices and preferable over other types of fuel cells. However, to avoid using expensive catalysts such as platinum or ruthenium, high temperature operation becomes an obligation which is one of the most common drawbacks of a SOFC. A typical SOFC is composed of three main compartments, an anode, an electrolyte and a cathode. Not only there is a need for compartments with similar thermal expansion coefficients, but also novel materials should be constructed to have a better capacity in a SOFC as well. Therefore, this study focused on the anode compartment and aimed to analyze its performance under different conditions. Since oxidation takes place in the anode part, increasing oxidation capacity could be an effective way to optimize the cells. To do so, a practical technique, impregnation, was applied to the anode part. Transition metals, manganese and vanadium with multiple oxidation states are selected. Possible increase in the oxidation capacity is one of the principle reasons why Mn and V are good candidates for impregnation. Both conventional and impregnated cells were characterized by X-Ray Diffraction (XRD), X-Ray Photoelectron Spectroscopy (XPS), Scanning Electron Microscopy (SEM) and their performance tests were implemented by Linear Sweep Voltammetry (LSV) and Electrochemical Impedance Spectroscopy (EIS). After characterization and performance tests, it has been concluded that as a practical technique, impregnation works well in this system under H_2 and CH_4 fuels and one can end up with a noteworthy enhancement of anode performance in the intermediate temperature range for a SOFC.

ÖZET

ORTA SICAKLIKTA ÇALIŞAN KATI OKSİT YAKIT PİLLERİ İÇİN MANGAN VE VANADYUM EMDİRİLMİŞ ANOT SİSTEMLERİ

Katı Oksit Yakıt Pilleri (KOYP), bir yakıtın oksitlenmesi ile kimyasal enerjiyi elektrik enerjisine dönüştüren çevre dostu elektrokimyasal enerji üreten cihazlardır. Yakıtın elektriğe dönüştürülmesinde sahip oldukları yüksek verimlilik ve çok çeşitli yakıtlara tolerans göstermeleri onları umut verici cihazlar haline getirmekte ve diğer yakıt pilleri türlerine göre tercih edilmektedirler. Bununla birlikte, platin veya rutenyum gibi pahalı katalizörleri kullanmaktan kaçınmak için, bir KOYP'nin en yaygın dezavantajlarından biri olan yüksek sıcaklıkta çalışmak bir zorunluluk haline gelmektedir. Tipik bir KOYP, anot, elektrolit ve katot olmak üzere üç ana bölmeden oluşur. Sadece benzer termal genleşme katsayılarına sahip bölmeler değil, aynı zamanda bir KOYP'de daha iyi kapasiteye sahip yeni malzemeler de inşa edilmelidir. Bu nedenle, bu çalışma, anot tarafı üzerinde yoğunlaşmış ve anot kompartmanının performansının değişik koşullarda incelenmesi amaçlanmıştır. Oksidasyon anot bölümünde gerçekleştiğinden dolayı artan oksidasyon kapasitesi, hücrelerin optimize edilmesi için etkili bir yol olabilir. Bunu yapmak için, anot kısmına pratik bir teknik olarak, emdirme işlemi uygulanmıştır. İlk olarak, çoklu oksidasyon durumlarına sahip bir geçiş metalleri, mangan ve vanadyum seçilmiştir. Oksidasyon kapasitesindeki olası artış Mn ve V'nin iyi bir aday olmasının temel nedenlerinden biridir. Geleneksel ve emdirilmiş hücreler, X-Ray Diffrasyon (XRD), X-Işını Fotoelektron Spektroskopi (XPS), Taramalı Elektron Mikroskobu (SEM) ile karakterize edilmiştir ve bunların performans testleri Çizgisel Süpürme Voltametri (LSV) ve Elektrokimyasal Empedans Spektroskopisi (EIS) uygulanmıştır. Karakterizasyon ve performans testlerinden sonra, pratik bir teknik olarak, emdirme işleminin bu sistemde H_2 ve CH_4 yakıtları altında iyi sonuç verdiği ve KOYP için orta sıcaklık aralığında anot performansının kayda değer bir artış olduğu sonucuna varılmıştır.

TABLE OF CONTENTS

LIST OF FIGURES

LIST OF TABLES

LIST OF SYMBOLS

f	Frequency
θ	Diffraction angle in X-Ray Diffration analysis
λ	The wavelength of electromagnetic radiation
ϕ	Work function of the spectrometer
ω	Radial frequency
Φ	Phase difference
Å	The length equal to 10^{-10}
δ	Doping level
η	Polarization

LIST OF ACRONYMS/ABBREVIATIONS

3D	Three Dimensional
AC	Alternating Current
AF	Activation of Fuels
AFC	Alkaline Fuel Cell
APU	Auxiliary Power Unit
ASR	Area Specific Resistance
BSE	Back-Scattered Electrons
C	Capacitance
CHP	Combined Heat and Power
CPE	Constant Phase Element
CT	Charge Transfer
DC	Direct Current
Diff	Diffusion of Species
EDS	Energy-dispersive X-Ray Spectroscopy
EIS	Electrochemical Impedance Spectroscopy
ESCA	Electron Spectroscopy for Chemical Analysis
ESEM	Environmental Scanning Electron Microscopy
GDC	Gadolinum Doped Ceria
I-V	Current-Voltage
IT-SOFC	Intermediate Temperature Solid Oxide Fuel Cell
L_b	Inductance
LSCF	Lanthanum Strontium Cobalt Ferrite
LSGM	Doped Lanthanum Gallate
LSM	Lanthanum Strontium Manganite
LSV	Linear Sweep Voltammetry
MCFC	Molten Carbonate Fuel Cell
OCV	Open Circuit Voltage

ORR	Oxygen Reduction Reaction
PAFC	Phosphoric Acid Fuel Cell
PEMFC	Polymer Electrolyte Fuel Cell
Q	Constant Phase Element
R	Resistance
R_b	Bulk Resistance
RQ	Resistance & Constant Phase Element Circuit
sccm	Standard Cubic Centimeters per Minute
ScSZ	Scandia Stabilized Zirconia
SDC	Samaria Doped Ceria
SED	Secondary Electron Detector
SEI	Secondary Electron Imaging
SEM	Scanning Electron Microscopy
SOFC	Solid Oxide Fuel Cell
TEC	Thermal Expansion Coefficient
TPB	Triple Phase Boundary
XPS	X-Ray Photoelectron Spectroscopy
XRD	X-Ray Diffraction
YSZ	Yttria Stabilized Zirconia

1. INTRODUCTION

1.1. Energy Dilemma

Energy, the capacity to do work [1]; can be described as the driving force of life and may exist in different forms. There has been and will always be an endless requirement for energy in this universe. However, with high population growth rate and limited sources of commonly used energy suppliers, the need for efficient energy production has become a vital issue to be solved. To do work, many sorts of energy are used and these sources are classified mainly as renewables and non-renewables.

Most of our energy comes from non-renewable energy sources which two examples of them are coal and petroleum. While using these sources for instance burning fossil fuels, carbon emissions and other chemical pollutants are inevitable problems and eventually cause global warming and climate change. Besides, renewable energy sources are of great interest to governments and are being utilized nowadays, but the effort towards renewable and sustainable energy is not enough to meet rising demands. Even though there are ways to enlarge the usage of renewable energy sources such as wind and sun, they are intermittent energy suppliers that supply energy when it is not needed and fail to provide it when needed. That brings the complication of storing energy on stage. Extensive research to store and transform energy is another way to deal with energy dilemma, yet it may take much time to construct and spread such technologies.

Batteries and capacitors do energy storage on a large scale at the present time, and making use of them in principle support the struggle to match the demand and supply for energy. For batteries, the possibility of contaminating environment by leaking heavy metals forces scientists to generate more efficient ideas and find innovative routes to produce energy without threatening the environment. In addition to efficiency, lifetime should be considered as well and unfortunately most batteries have short lifetimes.

1.2. Fuel Cells

Fuel cells are electrochemical devices that can convert chemical energy to electrical energy by oxidizing a fuel. The invention of fuel cells dates back to 1838 when the inverse electrolysis idea was proposed by Christian Friedrich Schönbein and regarded as fuel cell effect [3]. Shortly after, William Robert Grove discovered a cell which is named after him and in which he used zinc and platinum electrodes in 1839. He also invented gas voltaic battery that can be regarded as the pioneer of modern fuel cells [4]. Later in time, Charles Langer and Ludwig Mond performed experiments with air and coal gas and revealed the term “fuel cell”.

Depending on the type, fuel cells exhibit higher efficiencies (from 40% up to 80%) compared to ordinary methods of generating power and in addition to this, they have considerably high lifetimes.

Every fuel cell has two electrodes: anode and cathode. Third component is an electrolyte, which separates anode and cathode. At the anode, a catalyst takes the electrons of hydrogen atoms and leaves positively charged hydrogen ions, in other words it oxidizes the fuel, such as hydrogen or methane. At the cathode, again by the aid of a catalyst, oxygen is reduced and the hydrogen ions combine with oxide ions to produce water that then flows out of the cell. In this scenario, electrolyte acts like a salt bridge and transports oxide ions formed at the cathode.

Fuel cells are categorized primarily by the kind of electrolyte they use. This difference in electrolyte type results in different working conditions for each fuel cell type. Accordingly, they have various advantages and disadvantages based on their individual conditions. The general properties are summarized in Table 1.1. including alkaline fuel cell (AFC), polymer electrolyte membrane fuel cell (PEMFC), phosphoric acid fuel cell (PAFC), molten carbonate fuel cell (MCFC), solid oxide fuel cell (SOFC). Among these, SOFCs are having tremendous attention from researchers nowadays because of their better performance, relatively high stability and compactness.

Table 1.1. Types of Fuel Cells.

Fuel Cell	**AFC**	**PEMFC**	**PAFC**	**MCFC**	**SOFC**
Charge Carrier	OH^-	H^+	H^+	CO^{2-}	O^{2-}
Electrolyte	KOH	Nafion	H_3PO_4	Li_2CO_3 + K_2CO_3	ZrO_2 + Y_2O_3
$T_{operation}$ (^oC)	100	80	200	650	650-850
Fuel Type	Pure H_2	Pure H_2	Pure H_2	H_2, CO, CH_4	H_2, CO, CH_4
Efficiency	50-70%	35-60%	35-50%	40-55%	45-60%
Application Areas	Military Space vehicles	Electric utility, Portable power, Transportation	Electric utility	Electric utility, Distributed Generation	Electric utility, Auxiliary Power, Distributed Generation

1.3. Solid Oxide Fuel Cells

As an energy conversion device, a solid oxide fuel cell provides electrical energy from fuel oxidation and is not restricted to Carnot cycle because of not being a heat engine. As a consequence, CO, NO_x, and other pollutant emissions become negligible compared to internal combustion engines with only 18% efficiency [5].

SOFCs have become of great interest due to their high operation temperature and fuel management. During operation, they need continuous fuel flow for instance hydrogen gas flow and oxidant such as oxygen in the air in order to react and then to generate electricity at

high operation temperatures. Oxidation of the fuel takes place in the anode part while oxidant is reduced in the cathode part. In order for the cycle to be completed, oxide ions from cathode are transferred towards anode and electrons in the external circuit move from anode to cathode. As a by-product water is given off out of the system.

Unlike the other types of fuel cells, SOFCs can have several geometries. A planar fuel cell is composed of three flat components, where anode and cathode are placed on two sides of the electrolyte. It is also possible to construct an SOFC in a tubular design where electrolyte has a cylindrical shape and anode and cathode are placed on two sides to have contact with the fuel flow and the oxidant respectively. As for the performances, the planar geometry is better since the planar design exhibits lower resistance [6]. A third geometry is named as modified planar fuel cell design where instead of having the conventional flat surfaces for compartments, there is a wave-like structure with high durability [7].

Because the output voltage from a single cell cannot exceed 1 V, not only a single cell is operated but also a series of cells up to hundreds is connected to achieve the production of high electricity at high temperatures, which is referred to as SOFC stack. Although high temperature enables state of art SOFC stacks better tolerance to the impurities, materials used in the system becomes thermally vulnerable during operation.

1.3.1. Application Areas

In comparison with other sorts of fuel cells, SOFCs offer much higher power densities. One of the rapidly developing application areas of planar SOFC systems is the residential combined heat and power (CHP) designs. For improved application systems, lowering temperature and thus shortening the start-up and shut-down processes, also enabling durable constructions would make lower temperature SOFCs a suitable technology for mobile applications such as transportation vehicles [8].

SOFCs have been utilized as auxiliary power units (APU) for providing electrical power to aircrafts. Water produced during operation of these SOFCs may also be utilized by aircrafts

when necessary [9]. Furthermore, one of the fundamental focus areas concerning SOFC applications is to design integrated coal gasification SOFC power systems [10].

1.3.2. Reactions and Working Mechanism

As mentioned above, cathode reduces the oxygen from air by the aid of the electrons from the external circuit and leaves oxide ions (O^{2-}) to electrolyte:

$$O_2\,(g) + 4e^- \rightarrow 2O^{2-} \tag{1.1}$$

At the anode H_2, CO or CH_4 as fuel is oxidized and electrons are liberated to the external circuit:

$$H_2\,(g) + O^{2-} \rightarrow 2H_2O(g) + 2e^- \tag{1.2}$$

$$CO\,(g) + O^{2-} \rightarrow CO_2\,(g) + 2e^- \tag{1.3}$$

When the fuels containing hydrocarbons such as CH_4:

$$CH_4 + 4O^{2-} \rightarrow 2H_2O + CO_2 + 8e^- \tag{1.4}$$

A planar SOFC consisting of three main components with chemical, morphological stability, and mechanical compatibility can be demonstrated as in Figure 1.1. Cathode part that is subjected to air containing oxygen has porous structure for air to flow as well as catalytic activity for oxygen dissociation. On the other hand, anode possessing porous material for fuel flow is available for electrochemical oxidation of H_2, CO or other fuels to produce free electrons and water is formed when combining with oxide ions. Electrolyte as the ionic conductor has the role of being a bridge for only oxide ions produced in the cathode and prevents the passage of free electrons. On the nature of this concerted mechanism, electricity is produced via low cost compartment materials at high temperatures.

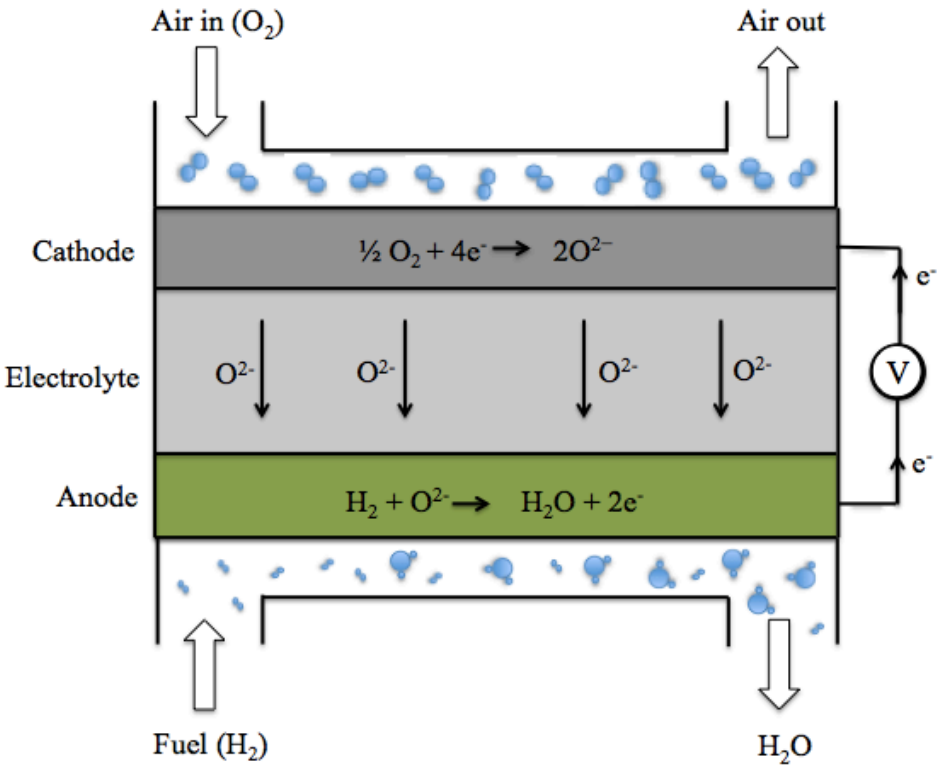

Figure 1.1. Schematic illustration of SOFC working mechanism.

Due to cell efficiency decrease resulting from the decrease in fuel concentration, outlet gas may still have valuable fuel and this brings us to constructing an SOFC system in order to utilize the fuel at its best level and optimize all the parameters in the system [11]. Nernst Equation directly affects the voltage of a fuel cell and thus the power output. Open circuit potential can be determined by the Nernst Equation, which takes into account the Gibbs free energy of the reaction and partial pressures of reactants and products.

1.3.3. Materials for SOFC components

An SOFC is made up of two porous electrodes and one dense electrolyte positioned between two electrodes. Porous electrodes are exposed to air and fuel, whereas dense electrolyte conducts oxide ions only and this allows an SOFC to operate at elevated

temperatures. However, high operation temperature gives rise to durability problems of the cell components. Owing to the mismatch in the thermal expansion coefficient (TEC), manufacturing low cost and symphonious materials with compatible TECs of the compartments in order for decreasing instable system and cracked cell possibilities has been of vital importance for SOFC technology.

1.3.3.1. Anode. The anode cermet comprises a composite of Yttria Stabilized Zirconia (YSZ) as ceramic (cer) material and Nickel as metal (met). It is the fuel electrode of an SOFC where the gaseous fuel oxidizes electrochemically after combining with the oxide ions coming from electrolyte. There has been great argument on if hydrogen oxidation takes place via hydrogen diffusion to YSZ or oxygen diffusion to nickel. Yet, it is proven that none of these mechanisms is valid; the oxidation takes place on the oxygen atoms in the interface of Ni and electrolyte material [13]. It is a special interface area called Triple Phase Boundary (TPB) where the anode, electrolyte and fuel meet. The idea of enhancing the reaction rate and oxidation ability through anode is provided by increasing the active area, also known as TPB. Moreover, research is being done on 3D imaging to observe TPB densities as a route of detecting the cell performance [12].

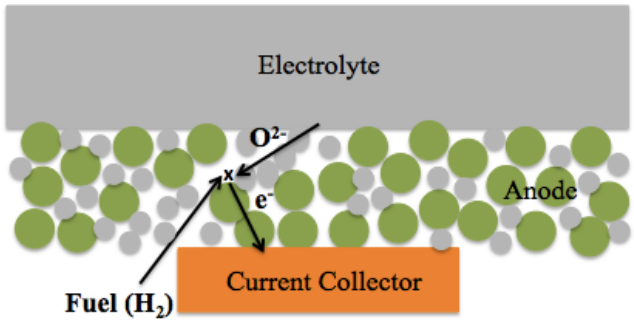

Figure 1.2. Schematic illustration of Triple Phase Boundary for anode.

As it is seen in Figure 1.2, dense electrolyte conducts oxide ions, fuel passage is possible through porous material of anode and lastly current collector collects produced free

electrons and then conveys them to the external circuit. For this reason, electrolyte material can be mixed with anode so as to increase active sites of TPB areas.

$$H_2(g) + O^{2-} \rightarrow 2H_2O(g) + 2e^- \quad (1.5)$$

One of the significant advantages of SOFCs is that they employ non-precious metals and ceramics, yet the cell efficiency is still high. A wide variety of metals (Cu, Ni, Co, Fe, Mn, Ag, Pd, Rh, Ru, Au, Pt) have been investigated for an anode metal catalyst material and consequently Nickel metal showed optimal catalytic activity. Ni has electron acceptor capability and in addition to this it can dissociate hydrogen leaving hydrogen protons towards electrolyte [14].

Although Ni anodes are the most commonly used anode materials with advantageous properties such as high catalytic activity, electrical conductivity, and good thermal stability at high temperatures; they suffer from carbon deposition (i.e., coking) and sulfur poisoning while utilizing hydrocarbon fuels. Because Ni is also a catalyst for carbon deposition, methane cracking (Equation 1.5) may take place during operation and cause irreversible microstructural damage in an anode system.

$$CH_4 \rightarrow C + 2H_2 \quad (1.5)$$

$$2CO \rightarrow CO_2 + C \quad (1.6)$$

Deposited carbon resulting from dehydrogenation reaction of hydrocarbons (Equation 1.5) at high temperatures will cover the Ni surface and TPB for anode oxidation will be blocked causing deterioration in cell performance [15]. Suppressing carbon deposition is performed by reducing operation temperature of cells, diluting hydrocarbon containing fuel streams or exposing fuel with large amounts of steam (>60 vol%). However, raised amount of steam in fuel may reduce cell efficiency [16,19]. Another solution to avoid carbon deposition could be producing novel anode materials by changing the anode material composition. For instance, introducing anode with BaO and CeO_2 has an effect on coking resistance by

providing a solution for coking removal [17]. Since carbon deposition routes for CH_4 and CO differ from each other, morphologies and reaction mechanisms have to be investigated individually. As to deposition problem in CO case (Equation 1.6), it has been observed that keeping the anode under moderate current densities during dry CO exposures mitigated the harmful effects on anode [18].

As for the second problem regarding Ni anodes, agglomeration impairs Ni particles and TPB length after the reduction [15]. Ni agglomeration, in other words Ni grain growth causes a loss in percolation of anodes and results in a performance drop. Solution to this problem could be making changes in the fabrication process. Consolidated NiYSZ anode fabricated with particles of certain sizes resulted in a stable material. Wet impregnation of Samaria-doped Ceria (SDC) or YSZ into Ni/YSZ anode has also led to an enhanced electro-catalytic activity and inhibited agglomeration of Ni particles at high temperatures [20].

Instead of Ni, Copper (Cu) has been examined for anode compartment of SOFCs; as Cu was known to be not susceptible to coking while utilizing fuels such as methane or syngas. Tests were implemented and the obtained performance demonstrated promising results. Having said that, copper has its own drawbacks that one of them is low melting point of 1083^0C, which restricts the operation temperature, whilst melting point of Ni is 1453^0C. Secondly, it is not a powerful catalyst for C-H and C-C bond breaking; therefore one needs to add another catalyst such as Ce to enhance the oxidation performance where Cu acts only as electrical conductivity agent [21].

1.3.3.2. Electrolyte. The electrolyte part of an SOFC is a dense ceramic material that is responsible for conducting oxide ions and has negligible electrical conductivity. Unlike electrodes, electronic conductivity is not desired for good electrolytes and should be kept as low as possible to prevent leakage currents. In addition, unless there is a good ionic conductivity in a dense electrolyte, no current flow through the cell but only potential difference would be observed.

Yttria Stabilized Zirconia (YSZ) is the most widely used electrolyte material containing 8 mol % Y_2O_3 + 92 mol % ZrO_2. Doping of Y_2O_3 to ZrO_2 creates holes named oxygen vacancies and oxide ion transportation through the electrolyte material occurs via oxygen vacancy path. The optimal operating temperature for YSZ is between 800-1000^{0}C and that brings material compatibility problems as well as the question of keeping temperature low while the ionic conductivity is still gratifying. Scandia Stabilized Zirconia (ScSZ) and some other novel electrolyte materials have so far been built to have ionic conductivity values at lower temperatures. ScSZ usually with 9 mol % Sc_2O_3, doped lanthanum gallate (LSGM) and Gadolinium Doped Ceria (GDC) are used as electrolyte materials for SOFCs as well [21]. The thickness of an electrolyte between electrode compartments should be as thin as possible for ideal performances; even so, it has to have an adequate thickness not to injure the cell arrangement as a whole [22].

1.3.3.3. Cathode. High electrical conductivity, catalytic activity, compatibility with other compartments and effective mobility of oxygen ion can be considered as desired properties for a cathode, also known as air electrode. Employing porous materials is crucial to optimize the allowance of airflow through the cathode material where the electrolyte as ionic conductor, the cathode as electronic conductor and the oxygen from air are in contact (TPB) (Figure 1.3). While operation, adsorbed O_2 from air is reduced on cathode surface and generated oxide ion travels through electrolyte material.

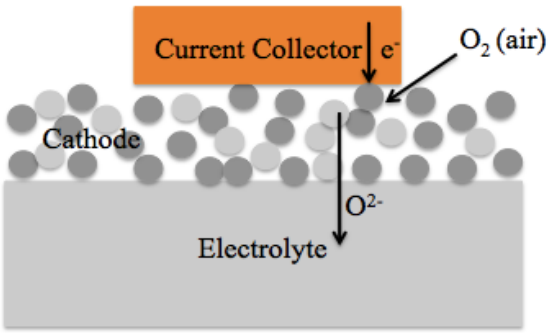

Figure 1.3. General schematic illustration of Triple Phase Boundary for cathode.

As mentioned above, the general representation of cathode reaction is as follows:

$$O_2\,(g) + 4e^- \rightarrow 2O^{2-} \tag{1.7}$$

However by using Kröger-Vink notation (Equation 1.7), one can interpret the scenario deeply in cathode compartment.

$$O_2\,(g) + 4e' + 2V_O^{\bullet\bullet} \rightarrow 2O_o^x \tag{1.8}$$

Where O_2 is the oxygen coming from air and e' represents the free electrons transported from anode, $V_O^{\bullet\bullet}$ shows the doubly charged oxygen vacancy and lastly O_o^x is the oxygen ion produced in cathode. Kröger-Vink Notation works for anode reaction (Equation 1.9) as well. H_2 fuel is oxidized with oxide ions from cathode and leaves free electrons again to complete the circuit. At the end, the overall cell reaction is simply showed as in (Equation 1.10) [23].

$$H_2\,(g) + O_o^x \rightarrow H_2O + 2e' + V_O^{\bullet\bullet} \tag{1.9}$$

$$2H_2\,(g) + O_2 \rightarrow 2H_2O \tag{1.10}$$

In order to form oxide ions at the cathode, oxygen adsorption then reduction on cathode surface should take place first. The oxygen reduction reaction, abbreviated as ORR, has a slow reaction rate and that is the reason why catalysts are needed. Platinum catalysts are known to be most efficient catalysts for ORR; however, due to cost issues, immense research is now being done to establish novel materials. Some metals such Au, Rh, Ir etc. have been examined for a better oxygen reduction, yet their catalytic activities were poor than Pt and they do not exhibit electrochemical stability [24].

Perovskite structure, which is generally being used in cathode materials, is a type of crystal structure with a chemical formula ABX_3, where X atoms are generally oxygens, B stands for a comparatively smaller cation and A represents a larger metal cation [25].

Different perovskite based contents have been manufactured as cathode compartments depending upon the operation temperature region of a fuel cell. Composite cathodes containing both one ionic conducting and one electronic conducting oxide are preferred frequently. As far as the need for lower operation temperature due to durability issues is concerned, catalytically active novel cathode materials should be produced. Because the usual cathode materials $(La,Sr)MnO_{3+\delta}$ (LSM) and $(La,Sr)(Co,Fe)O_{3-\delta}$ (LSCF) operate at temperatures higher than 600^0C.

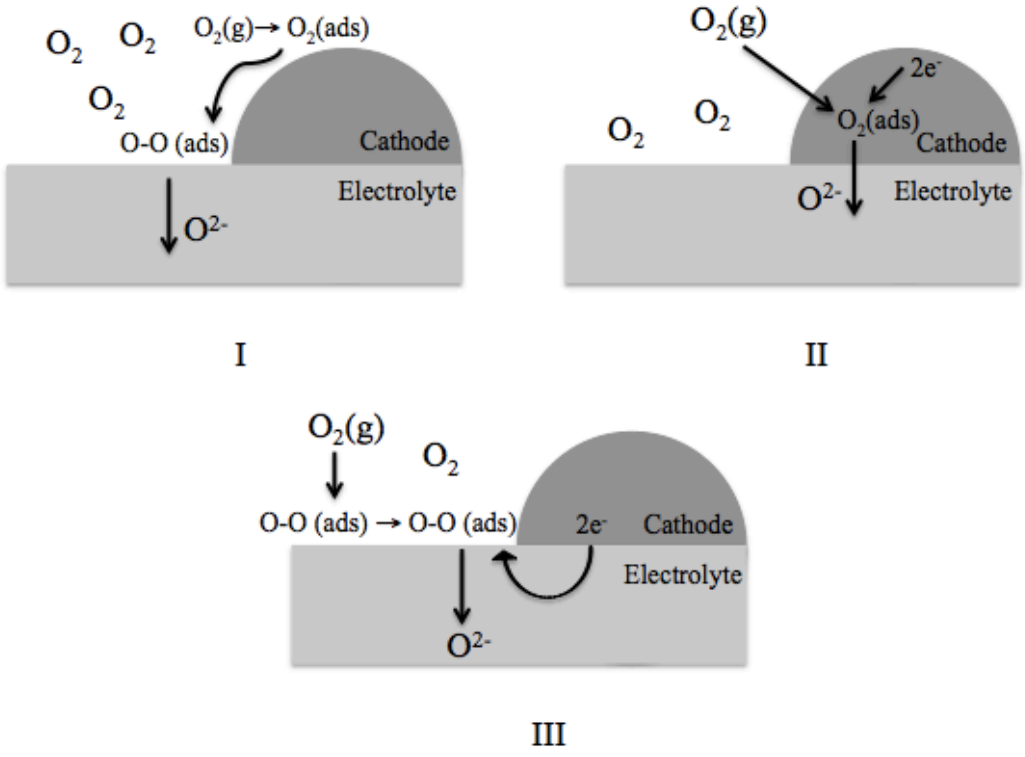

Figure 1.4. Three possible pathways for oxygen reduction in cathode, (I) Cathode surface pathway, (II) bulk pathway, and (III) electrolyte surface pathway.

Cathodes that contain electronically conductive perovskite type materials may provide different routes for oxygen reduction depending on the type of electrolyte material used. The surface pathway (I) is the most possible route, in case the pure electrode is utilized in cathode.

If a material with both ionic and electronic conductivity, such as Lanthanum Strontium Cobalt Ferrite (LSCF), is employed; the bulk pathway (II) is more likely to occur. And a composite material such as LSM/YSZ would end up with electrolyte surface pathway (III) as demonstrated in Figure 1.4 [26].

The ideal case for a working SOFC would seem like a straight line on current-voltage graph that indicates measured current value for a given voltage (Figure 1.5). No losses could be observed and voltage value would remain fixed, as it was when the cell operation started. However, in reality, different kinds of polarizations (losses) such as ohmic polarization, concentration polarization and activation polarization occur as long as the current is produced.

During operation, the voltage output (V) can be represented as:

$$V = E_o - IR - \eta_a - \eta_b \tag{1.11}$$

Where E_o is open circuit voltage (OCV), I is the current that is passing through the cell, R is the cell resistance, therefore the multiplication of I and R is the ohmic polarization, η_a is the concentration polarization, and η_b is the activation polarization as schematized in Figure 1.5.

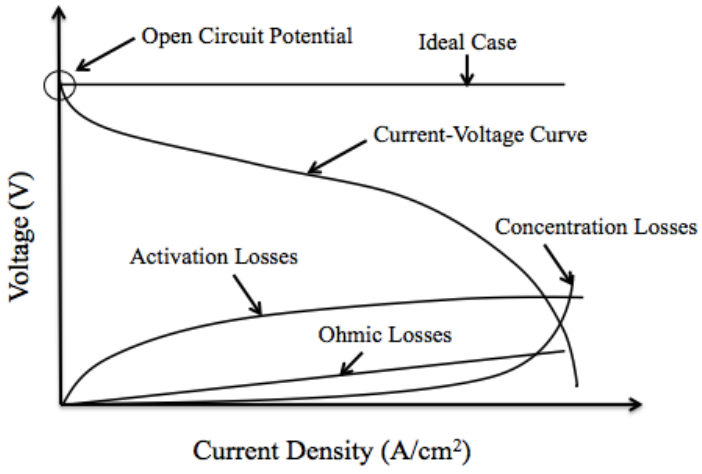

Figure 1.5. Current – voltage (I-V) curve of an SOFC.

Ohmic resistance loss results from the resistance of oxide ion flow in the electrolyte and the resistance of the electron flow in electrodes. As a solution, making use of thinner electrolytes with higher ionic conductivities and electrodes with high electronic conductivities may lessen the ohmic resistance.

Concentration polarization is induced by the active reaction areas, TPBs, owing to the outage of charge carrying reactants resulted from slow diffusion of fuel gas channels through the porous electrodes.

Activation polarization is the sacrificed voltage to pass the activation barrier for electrical current production, or to put it more explicitly; it is the voltage spent to drive electrochemical reactions towards favored direction.

1.3.4. Intermediate Temperature SOFCs

Because of the requirement for high temperatures in SOFCs, there will be a problem concerning the long period of time during warm up and cool down processes. In addition to long waiting hours for heating (12 hours and more), energy consumption to reach the temperatures higher than 800^{o}C is another disadvantage of conventional SOFC systems. As mentioned in previous sections; cathode, electrolyte and anode compartments are thin layers; and as a result, a thin single cell system becomes susceptible to cracks and fragility. These cracks, occurring either in the cell itself or the in sealants used, may spoil all the cell system or cause a non-negligible decline in the performance since the fuel or air could escape through the system and not reach the electrode surfaces efficiently.

After considering all of these handicaps owing to high temperature regime, moving to lower operation temperatures has become a trend among researchers. Proposed Intermediate Temperature range is between 500-800^{o}C and SOFCs operating in this region are named as Intermediate Temperature Solid Oxide Fuel Cells (IT-SOFC).

Intermediate operation temperature provides more choices for materials and different geometries that can be utilized, lowers the corrosion possibility of metallic components, and reduces the system cost. Faster heat up and cool down processes also enable applicants to extend the use of IT-SOFCs in mobile applications. Depending on application area the most suitable operation temperature will change; hence, there is no such value that one can regard as the optimum temperature for SOFCs. Yet, going down towards intermediate temperatures is still of prime importance as it unlocks many doors respecting efficiency and handicaps turn into advantages.

To do so, two particular pathways can be followed to attain high performances at low temperatures. First, by reducing the electrolyte thickness, area specific resistance (ASR) of the fuel cell may be lessened and as a second pathway new material that can promote ionic conductivity in electrolyte and enhance performance of electrodes may be produced [27].

1.4. Material Characterization

Material characterization of SOFCs is usually carried out as a process for checking the quality of fuel cells before and after the electrochemical operations. Characterizations also provide inclusive information about material morphologies, electrode porosity and distribution, interfaces of electrolyte and electrodes, layer adherence of compartments, crystal structures, phase composition, and oxidation states of elements as significant parameters.

Material characterization is conducted by multiple analysis techniques such as X-Ray Diffraction (XRD), X-Ray Photoelectron Spectroscopy (XPS), Scanning Electron Microscopy (SEM) and etc. that can pave the way for evaluating the material properties thoroughly.

1.4.1. X-Ray Diffraction (XRD)

To have in-depth information about crystal structures and compositions, XRD analysis is used as a non-destructive way of detecting atomic and molecular structures. Incident X-Rays are directed to the sample and diffracted with an angle that is characteristic for every

crystal structure (Figure 1.6). A detector analyzes reflected angle and depending upon the reflected angle, one can specify the crystal structure based on the database of all surveyed lattices by that time.

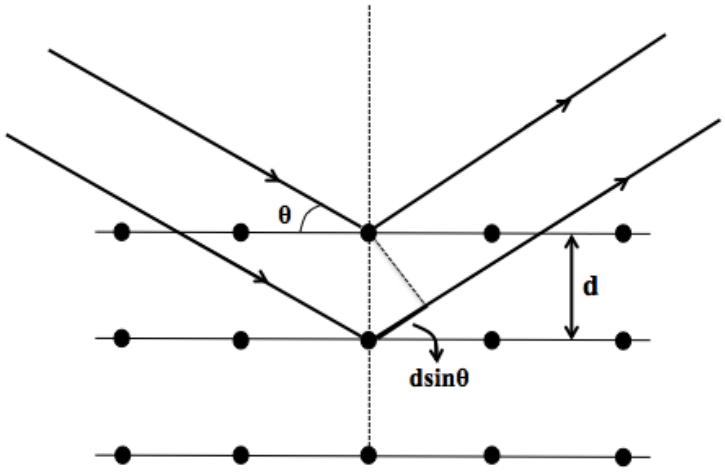

Figure 1.6. Schematic representation of the interaction between X-Rays and the sample.

X-rays are generated in a cathode ray tube, filtered to become monochromatic radiation and directed towards the sample to be analyzed. The interaction between the coming X-Rays and the sample develops constructive interference when the equation of Bragg's Law (Equation 1.12) is satisfied.

$$n\lambda=2d \sin \theta \tag{1.12}$$

In this equation, λ, as the wavelength of electromagnetic radiation is related with the diffraction angle (θ) and spacing of the lattice (d) in the analyzed sample. The detector measures the intensity of diffracted X-Rays continuously and this intensity value gives clues about the majority of particular crystal patterns [28].

1.4.2. X-Ray Photoelectron Spectroscopy (XPS)

As one of the standard ways of surface characterization, photoelectron spectroscopy involves photo-ionization and kinetic energy dispersion of the emitted photoelectrons to work the composition and examine core-levels of the surface of a sample by utilizing X-rays in ultra high vacuum chamber. In XPS, a photon excites an electron in a molecule or solid; or in other words, photons provoke the emission of electrons from inner shells. An energy analyzer scales the kinetic energy of emitted electrons and photoelectron spectrum can thus be assigned (Figure 1.7).

The photoionization process can be systematized by the equation predicating on photoelectric effect (Equation1.13):

$$KE = h\nu - BE - \phi \tag{1.13}$$

Where h is Planck's constant, ν is the frequency of ionizing light and hence hν is the energy of incident X-Rays, BE is the binding energy of ejected electrons, ϕ stands for the work function of spectrometer and KE is the kinetic energy of ejected electrons measured in XPS spectrometer. The ionization process is only possible in case the energy of photons is greater than the energy that holds the electrons within the structure. By this way; XPS, also referred to as electron spectroscopy for chemical analysis (ESCA), is able to measure the elemental composition, chemical state and hence the empirical formula of a substance except hydrogen [29].

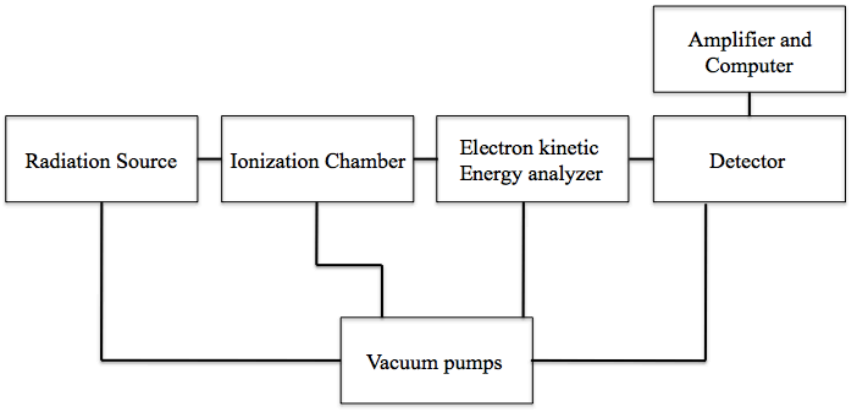

Figure 1.7. A block diagram of photoelectron spectrometer.

By evaluating the kinetic energy of the electrons ejected, binding energy can easily be found and knowing the binding energy of the electrons gives some clues about the material such as:

- The element that is the material is composed of,
- The orbital from which the electron is emitted,
- The environment of the atom where the electron is ejected [30].

1.4.3. Scanning Electron Microscopy (SEM)

Scanning Electron Microscopy (SEM) is a kind of electron microscopy that uses a beam of electrons bearing high energy to produce a variety of signals derived from the surfaces of samples. After reviewing the signals, detailed information can be revealed about the external morphology and orientation of constituents that make up the material. Commonly used imaging modes in SEM are secondary electron imaging (SEI) and back-scattered electrons (BSE). The former pictures the surface topography and surface morphology of samples in a wide spread manner because produced electrons interact with the near-surface regions, whereas the latter is used to show the contrast in a composition by reflecting electrons from

the specimen by means of elastic scattering. Since the intensity of back-scattered electrons is strongly associated to atomic number of the sample, BSE enables information about the weight dispersion of elements in the material. However, the fact remains that conventional SEM analysis demands a medium under high vacuum for samples to be pictured by the reason of a gaseous environment readily weakens electron beams and thus damages the analysis [31].

There is no doubt concerning the breadth of applications of SEM; nevertheless, some organic materials or volatiles are not suitable for performing this method. That is why a special instrumentation with low vacuum called Environmental Scanning Electron Microscopy (ESEM) delivers solution for this particular problem.

Most SEMs have an X-ray detector, Energy-dispersive X-Ray Spectroscopy (EDS), which is integrated into a SEM instrument. It works based on the principle that triggers the emission of radiation by ejecting an electron from its shell. After creating a hole via ejection, another electron from the higher energy shells fills the hole and the energy is released in X-Ray radiation form based upon traveling from a higher energy state to a lower one. The amount of released energy is quantified by energy dispersive spectrometer and specifies the elemental composition of the sample [32].

1.5. Performance Tests

In order to explore the performances of fuel cells and to observe possible enhancements or declines in fuel cell performance, there are several ways of testing. Linear Sweep Voltammetry (LSV) and Electrochemical Impedance Spectroscopy (EIS) are widely used kinds of performance testing methods for this purpose.

1.5.1. Linear Sweep Voltammetry (LSV)

Cell performance decreases from its ideal potential value due to multiple types of irreversible losses such as ohmic polarization, concentration (mass-transport related) polarization, and activation polarization as it was shown in Figure 1.5. These polarizations are

frequently defined as loss, overvoltage or over potential as well. In current-voltage (I-V) curve, in other words LSV diagram, it is easier to distinguish the polarization regions one by one at low operation temperatures. At higher temperatures, activation loss is less influential and for this reason, curvatures to the left cannot be observed clearly in the I-V curve whereas the curvatures to the right that are related to concentration losses are more apparent.

LSV is an electro-analytical method where the information acquired is measured current at a working electrode as the potential between working electrode and reference electrode varies [33]. In addition, as the third parameter, the scan rate that can vary from mV/sec to 10^6 V/sec may be altered by setting the time scale while sweeping as shown below in Figure 1.8.

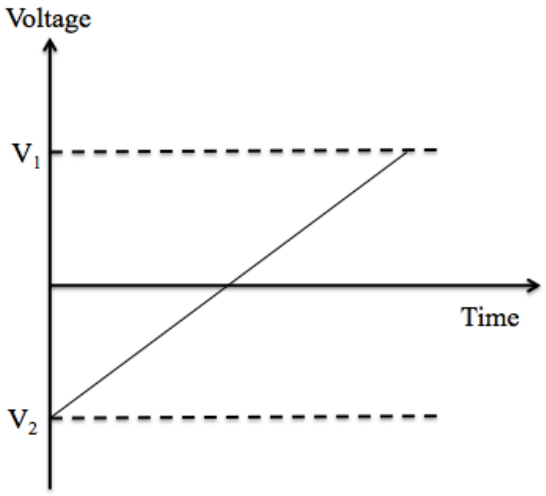

Figure 1.8. Voltage vs. time graph.

Furthermore, the properties of the linear sweep voltammetry (volt-ampero-metry) depend on several factors, such as the speed of electron transfer reactions, the chemical activity of electro-active species, and the rate that the voltage is scanned [34].

1.5.2. Electrochemical Impedance Spectroscopy (EIS)

Impedance spectroscopy varies from most of the voltammetric modes such as LSV and potential step methods, in that only disturbance is applied to the electrochemical cell. It is a forceful approach for looking into electrochemical systems and their procedures. The main strength of EIS lies behind its ability to question the relaxation phenomena where time scales range multiple orders of magnitude from minutes down to microseconds. In Linear Sweep or potential step methods, electrodes are driven to a condition far from equilibrium. On the contrary, impedance techniques depend upon perturbation of the electrochemical device with small magnitude alternating signals so that analysis can be done at equilibrium or in steady state. These small shocks given to the system can be applied current, applied potential and etc.

In case the sinusoidal shocks of the applied voltage is considered, Equation 1.14 can be used:

$$V(t) = V_0 \sin(\omega t) \tag{1.14}$$

Where $V(t)$ is voltage at t, V_0 is the amplitude of voltage, and ω is radial frequency. In the meantime, Equation 1.15 is the relationship between the radial frequency and the frequency f.

$$\omega = 2\pi f \tag{1.15}$$

The response of current $I(t)$ will be shifted in phase (Φ) and will also be sinusoidal with the same frequency (Figure 1.9), then equation becomes as the one below (Equation 1.16), where I_0 is the amplitude of the current:

$$I(t) = I_0 \sin(\omega t + \Phi) \tag{1.16}$$

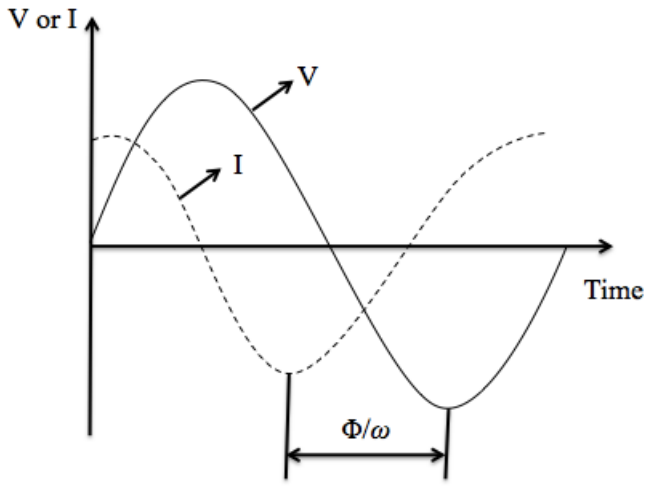

Figure 1.9. Sinusoidal voltage and current response.

$$R = V / I \tag{1.17}$$

In parallel with direct current situation that obeys Ohm's Law (Equation 1.17), the impedance is described as the value resulting from the division of voltage by current as in Equation 1.18.

$$Z = \frac{V\,(t)}{I\,(t)} \tag{1.18}$$

The impedance is a vector quantity; because it has a magnitude of Z_0 that is equal to V_0 divided by I_0, also has a phase difference between the voltage and current (Φ) (Figure 1.10). Therefore, it becomes more appropriate to state the impedance in complex notation (Equation 1.19).

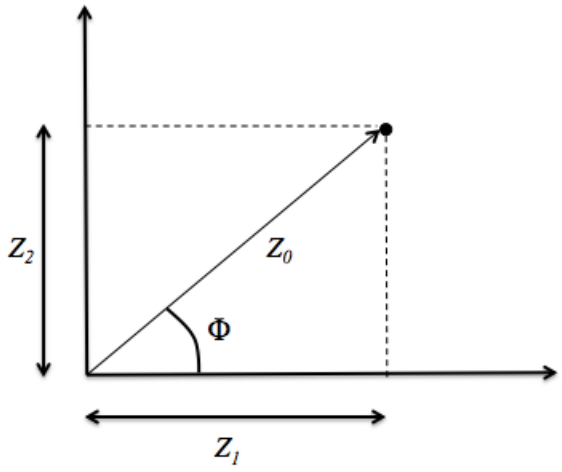

Figure 1.10. Impedance presentation in the complex plane.

$$Z = Z_0 (\cos \Phi + i \sin \Phi) = Z_1 + i Z_2 \tag{1.19}$$

Where $i = (-1)^{1/2}$, Z_1 is the real part of impedance and while Z_2 is the imaginary part.

$$e^{i\Phi} = \cos \Phi + i \sin \Phi \tag{1.20}$$

By using Euler's relationship (Equation 1.20), it is finally possible to extrapolate Equation 1.21:

$$Z(\omega) = \frac{V(t)}{I(t)} = Z_0 e^{i\Phi} = Z_0 (Z_{real} + Z_{imaginary}) \tag{1.21}$$

If the sinusoidal voltage is applied only to a resistor R, then Φ would be zero for all frequencies and Z_0 becomes entirely real as the way that the impedance turns into being completely imaginary when the sinusoidal voltage is applied only to a capacitor with phase angle $\Phi = -\pi/2$.

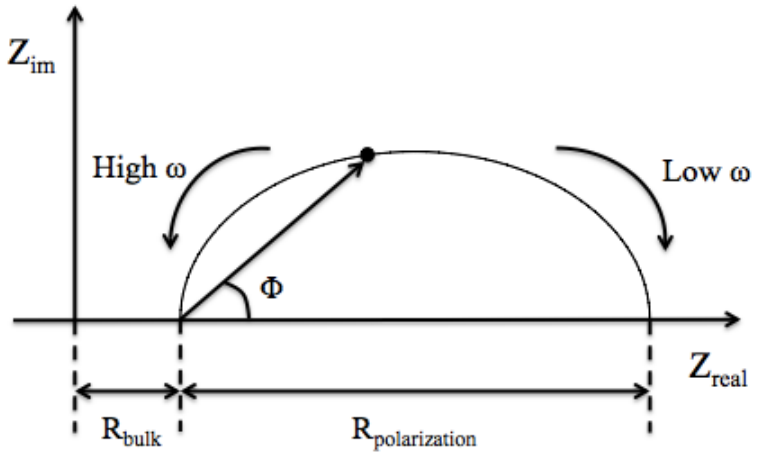

Figure 1.11. Schematic representation of Nyquist plot.

A complex curve, which is named as Nyquist plot (Figure 1.11), has confirmed very helpful for estimating impedance parameters appearing as several semicircles in the curve. Yet, by looking at a Nyquist curve, data presented does not give information about the frequency at specific points. As a vector quantity, impedance includes two parts as mentioned previously. Resistive process is represented on the x-axis and defined as Z_{real} while Z_{im} stands for capacitive process and is represented by a value on y-axis. The bulk resistance, R_{bulk} that can be seen from where the high frequency part intercepts with x-axis of the Nyquist Plot, is governed by the electrolyte and interconnects. R_{total} that is the intercept point at low frequency side is known as total resistance of the whole system. The subtraction R_{bulk} from R_{total} gives the polarization resistance $R_{polarization}$, which symbolizes all physical and chemical processes on cathode and anode [35].

1.6. Aim of the Study

There is not a shadow of doubt that the question referring to discrepancy of energy supply and demand remains to be one of the major issues of the universe. Apart from these, the energy dilemma does not comprehend the amount of energy that is available; instead, it

involves the arrangement in which the energy is available. Therefore, the ability to utilize energy by transforming it to an accessible form is the essence of all living creatures.

For allowing the large scale utilization of clean, inexpensive and reliable energy; an enormous effort should be put into changing the way of energy production that is still based on fossil fuels nowadays. As up-to-date source of future alternative energy, taking advantage of fuel cells could be advantageous rather than continuing with burning coal.

For this very reason, the scope of this thesis is focused on studying the anode compartment behavior of SOFCs under changing conditions. In this context, a functional method that is impregnation of anode with transition metals such as Mn and V has been aimed to strengthen the performance in intermediate temperature range. Along with the possible improvements in an entire fuel cell, impregnating anode with transition metals other than Ni could enable protection from coking and aggregation, since transition metals have a lot of oxidation states meaning they can carry oxygen that then captivate deposited C on anode surface.

A summary of the information including energy, fuel cells, SOFCs and its compartments is given based on literature review in Chapter 1, where one can also get core knowledge about material characterization and performance tests. In Chapter 2, experimental procedure of the study is explained in detail and deep discussion is made in Chapter 3 referring to acquired results depending upon advanced analysis techniques. Conclusion remarks on the enhancement of IT-SOFC performance thanks to transition metal impregnation are in Chapter 4 and future work of this study is mentioned in Chapter 5.

2. EXPERIMENTAL

2.1.Materials

As the experimental part of this study, 5x5 cm anode supported commercial solid oxide fuel cells obtained from Fuel Cell Materials Company were used to improve the anode performance. To do so, it has been benefited from manganese and vanadium salts, $Mn(NO_3)_2.6H_2O$ and Vanadium (III) acetyl acetonate purchased from Sigma Aldrich. Au wires (0.25 mm in diameter) obtained from Alfa Aesar and Au conductor paste obtained from Heraeus acted as current collectors. For sticking the cells, ceramic adhesive paste that is named as Aremco Ceramabond 552 was used.

2.2. Reduction of Cells

In the layered structure of planar SOFCs, the components are stiffly bonded to each other; hence, differences in properties of materials cause material strain resulting from the forced fixation of the cells. That is the reason why mechanical integrity is a vital aspect for trustable operation and stable thermal cycling of components. The mechanical properties of components have been deeply qualified in the past [36]. Yet, in the case of re-oxidation at elevated temperature because of lacking fuel gas due to sealant damage or fuel supply cut is still a perturbative possibility that seems to be unsolved. Under these conditions, fractures may occur due to oxidation and thus volume expansion of Ni particles that are dispersed in YSZ matrix. Additionally, cracks may be caused by the polarization resistance, which can be attributed to reduction and oxidation cycles [37]. When looking at this complication via macroscopic level, volume shrinkage and expansion during reduction and re-oxidation processes induce related stress on materials that can further cause irreversible fractures.

As it was patented in 1970s, Ni-ceramic composite materials have been used in the state-of-the-art anodes due to their low cost, high catalytic activity and electrical conductivity properties. However, while fabricating SOFCs, the anode part is sintered at high temperatures

(1300-1450^{o}C) leaving NiO particles inside the cermet. During reduction, the shrinkage of NiO is around 40%, and in the case of re-oxidation at high temperatures nickel expansion becomes around 66% in the absence of fuel as it can be observed in Figure 2.1. [37].

The reduction stimulates material shrinkage during the conversion of NiO particles to Ni metal and after re-oxidation the morphology of NiO particles alters compared with the initial sintered state (Figure 2.1). The porosity of anode layer is nearly zero at the end of sintering step. On the other hand, the reduction of NiO provides more space through the anode material as in the second illustration of Figure 2.1, since oxygen atoms are given off and Ni is smaller in volume compared to NiO. Sponge-like structure of re-oxidized state has more free space, which indicates the significant increase in the volume. Therefore, re-oxidation is an out of favor situation because of unmanageable manner of anode composition and it is almost impossible to prevent tensile strain, compressive stresses and, irreversible cracks in the system [38].

Despite all of the possible stresses on materials stated above, to provide better fuel flow through anode, reduction of NiO to Ni metal is compulsory. In this study, commercially available 5x5 cm anode supported solid oxide fuel cells obtained from Fuel Cell Materials Company that are in sintered state, hence with NiO particles in anode part, were used. Before the operation and conducting performance tests, cells were broken in order to fit alumina tubes (Figure 2.2.). Cells were composed of Ni/YSZ as anode and the thickest layer (400 μm), YSZ as electrolyte (3 μm), LSM (Lanthanum Strontium Manganite) as cathode (12 μm) and GDC as a barrier layer (3 μm) between anode and electrolyte. Broken cells were placed inside an alumina tube separately without using ceramic adhesive paste and the reduction program was arranged to heat the cells 2^{o}C/min until reaching 800^{o}C under the fuel composition of 25% H_2 and 75% N_2. Later on, cells were kept waiting for 2 hours at 800^{o}C and cooled down again with 2^{o}C/min until they reach room temperature. At the end of the reduction program, cells get prepared to proceed further.

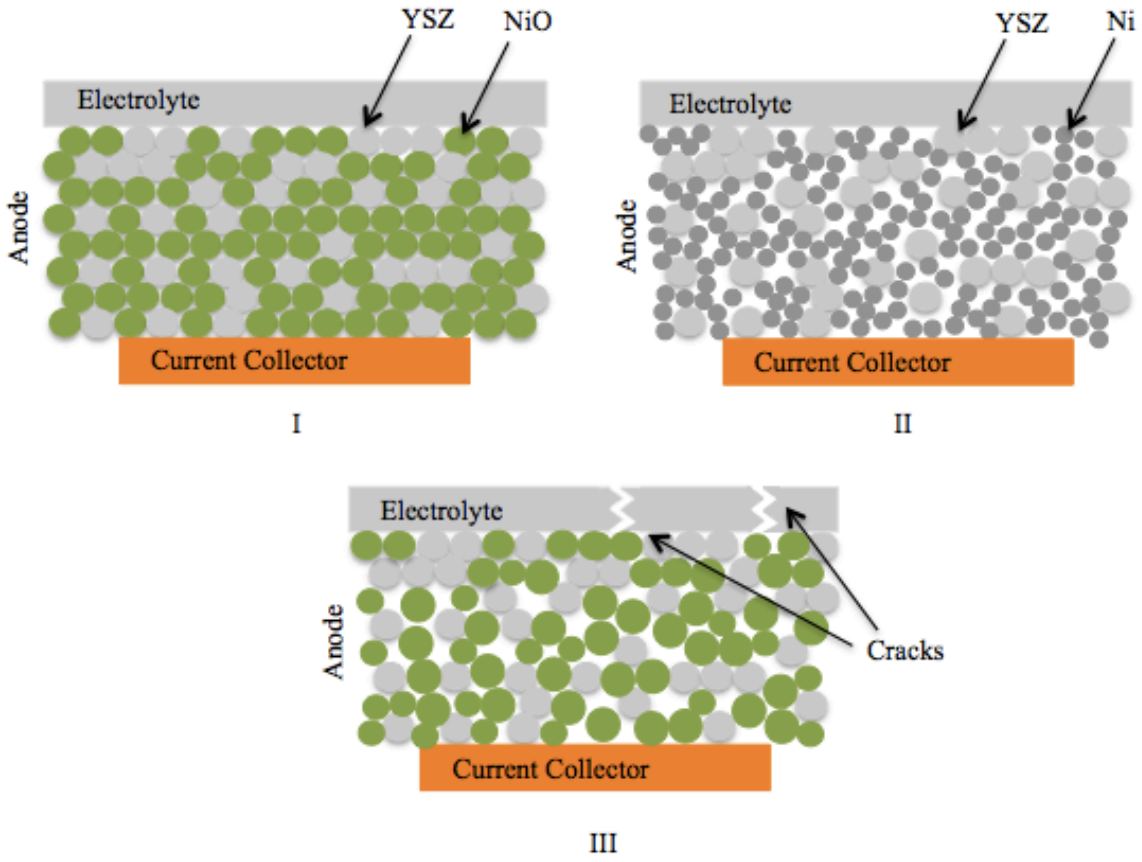

Figure 2.1. Schematic illustration of microstructural changes in Ni/YSZ based anodes during redox process: sintered state (I), reduced state (II), and first re-oxidized state (III).

2.3. Preparation of Set-up

After the reduction of NiO to Ni in the anode part, cells were ready for attaching gold wires as current collectors to electrodes (both anode and cathode layers) via gold conductor paste obtained from Heraeus. The second step contains sticking the cells with current collectors on top of a alumina tube with the help of adhesive paste (Aremco Ceramabond 552) in the way that cathode is looking upwards for being available to air contact and anode to fuel flow.

With the intention of not facing any fuel leakage problem, ceramic adhesive paste was mixed thoroughly prior to use and the alumina tube surface where the adhesive paste will be

applied was abraded and cleaned properly. In order to provide completely stable adhesion, paste was dried at room temperature for 1 hour, and step cured at 90°C and 200 °C for 2 hours at each temperature. Because the top of the alumina tube will lie within the furnace, current collectors had to be long enough to reach GAMRY Reference 3000 Potentiostat/Galvanostat outside the furnace. Fuel was supplied via copper pipes that are connected to mass flow controllers (Brooks 5850E) and exhaust gas outlet was enabled by syringe needle.

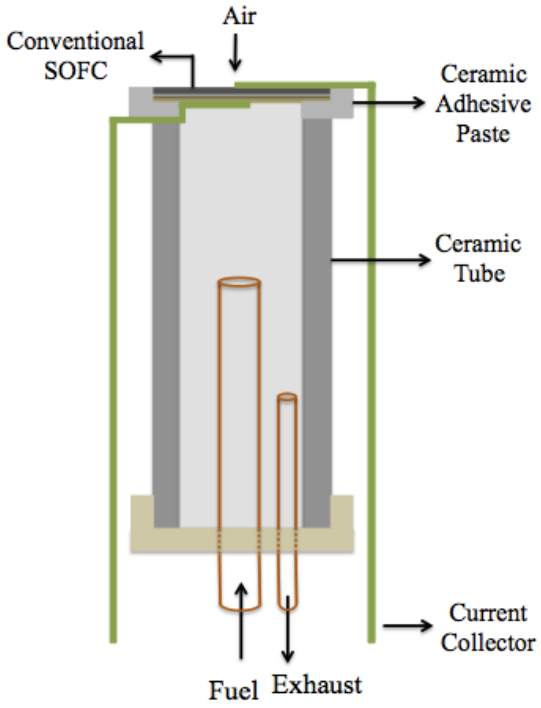

Figure 2.2. Experimental set-up of an SOFC.

2.4. Impregnation Technique

The development of solid oxide fuel cells operating at intermediate temperatures with several types of fuels requires the enhancement of electro-catalytic activity for the reduction of oxygen in cathode and the oxidation of fuels in anode. In this respect, wet impregnation is known to be a practical technique in the field of heterogeneous catalysis, since it comes up

with metal addition to the porous electrodes of SOFCs. The probable improvement in anode electrode makes wet impregnation method inviting and a triggering factor for researchers because of its easiness and great potential towards better operation of SOFCs. In spite of the fact that impregnation forms a basis for surprisingly better performances, it appears to be a rather recent phenomenon and only a few research is based on utilizing it and spreading its application [39].

In the present study, the notable impact of the impregnated oxide phase on the electro-catalytic activity and anode part is investigated in microscopic level. The impregnation of previously selected transition metal candidates Mn and V to anode part was carried out by placing two drops of $Mn(NO_3)_2.6H_2O$ and Vanadium(III) acetyl acetonate salts dissolved in distilled water. Both solutions were conducted to be 0.2 M and added drop wise on top of anode surfaces separately.

For Mn impregnation, 0.2870 g of $Mn(NO_3)_2.6H_2O$ was dissolved in 5 mL distilled water to end up with 0.2 M of Mn ions. Likewise for V impregnation, 0.3482 g of Vanadium (III) acetylacetonate was dissolved in 5 mL distilled water to have 0.2 M V solution. Solutions were dropped gradually on the anode part so as to investigate the effects of impregnation and manganese and vanadium oxides on the performance of the conventional (Ni-YSZ/YSZ/GDC/LSM) fuel cells by comparing the impregnated cells with non-impregnated (conventional) ones. By this way, the porous structure of Ni/YSZ anode layer absorbs solution and anode becomes a compartment that is composed of Nickel and Manganese or Vanadium at the end.

2.5. Instrumentation

Electrochemical Impedance Spectroscopy (EIS) and Linear Sweep Voltammetry (LSV) tests were carried out by Gamry Reference 3000 Potentiostat/Galvanostat device that is connected to a computer-controlled program for data accumulation.

X-Ray Diffraction (XRD) analyses were conducted with Rigaku D/MAX-Ultima+/PC Diffractometer using Cu-Kα radiation (λ=1.54056Å) at Boğaziçi University Advanced Technologies Research and Development Center where also XPS experiments were performed by Thermo Scientific K-Alpha Surface Analysis instrument. Al K Alpha X-Ray source with a spot size 400 μm was utilized. The step scanning was carried out from 0 to 90 degrees while measuring.

FEI-Phillips ESEM-FEG XL30 was used for the topography of cell layers via a variety of imaging techniques with multiple resolutions at Boğaziçi University Advanced Technologies Research and Development Center.

Lastly, Brooks 5850E was used as the mass flow controller in order to set certain composition for fuels flow.

2.6. Performance Evaluation and Calculations

Using polarization curves and electrochemical impedance spectroscopy has inspected the performance of the cells under different experimental conditions. Linear Sweep Voltammetry experiments were done to ascertain the polarization curves. With the intension of analyzing processes, reactions, ohmic, charge transfer and diffusion resistances, impedance data were surveyed in detail. Impedance spectroscopy provided the data by allowing investigation of a system by the reponse it produces in current or voltage after interfering a slight alternating current to a stationary state.

In this study, a data acquiring sequence was regulated in such a way that two LSV (polarization) curves were recorded in which between these two, four impedance measurements were implemented for 300mV, 200mV 100mV and open circuit voltage cases respectively. Thus, for every 50^{o}C from 400^{o}C to 800^{o}C, the regulated sequence that includes 6 different data recording steps was applied to observe the performance of the connected fuel cell described above. In Gamry Reference 3000 Potentiostat/Galvanostat device, anode of the cell was connected as the working electrode while cathode was connected as the counter

electrode. Measurement frequencies ranged from 100 kHz to 0.1 Hz and the amplitude of the AC perturbation was 20 mV.

Normalization of the polarization curves were done by dividing the current value to the area of the anode that was assigned to be 0.58 cm^2. In addition to that, impedance data was multiplied by 0.58 to get the Area Specific Resistance (ASR) value for the cells operated. Besides, power density calculations were done by multiplying voltage and current values that are read from the LSV results. After specifying the power densities, maximum power density values were also designated for each temperature as for the all calculation steps.

For the experiments done with H_2 fuel, the compositions were set to be 100 sccm (Standard Cubic Centimeters per Minute) H_2 and 20 sccm N_2 as carrier gas on anode side. For the experiments of CH_4 as fuel, mass flow controller was calibrated for CH_4 according to the fact that H_2 fuel supplies $2e^-$ to the circuit while CH_4 supplies $8e^-$. Also the equation of the mass flow controller for calibrations was used and CH_4 was set to be 32.60 sccm with the same amount of N_2, 20 sccm.

3. RESULTS AND DISCUSSION

In the junction point of being a battery and a heat engine, it is also possible to consider fuel cells as continuously fueled air-breathing devices [40]. Specific to solid oxide fuel cells and facilitating their applications, there is an urgent need for prospering performances to help scientists attain further overall accomplishments. Since the energy demand is rising in an accelerated manner, this sobering situation legitimatizes the necessity for more efficient energy conversion routes such that no greenhouse gasses are emitted and low-cost components are used.

To this end, the present thesis sets sight on an intention for the performance enhancement of anode compartment where the oxidation occurs. As an extension of the experimental part of the study, the characterization results will be discussed in detail in this chapter.

3.1. X-Ray Diffraction (XRD) Results

The X-Ray Diffraction data that is based on the crystal structure and the phase composition of samples was plotted depending on the results collected via Rigaku D/MAX-Ultima+/PC Diffractometer using Cu-Kα radiation (λ=1.54056Å) at Boğaziçi University Advanced Technologies Research and Development Center.

XRD results of the anode part of a conventional cell is illustrated in Figure 3.1 and taken as a reference for detecting the effects of wet impregnation of two transition metals, Mn and V. As the reference XRD result of a conventional cell that is purchased from Fuel Cell Materials Company, the expected major peaks of Yttrium Zirconium Oxide at two-theta values of 30^o, 35^o, 36^o, 50^o, 51^o, 59^o, 60^o, and 82^o can be observed. When it comes to Ni and NiO, the ones at 45^o, 52^o, 76^o are specific for Ni and NiO is represented at 63^o by a very small peak in other words with a low intensity. This indicates that after reduction process, a large

quantity of NiO is reduced to Ni metal that is a satisfactory result as it was aimed in the experimental part.

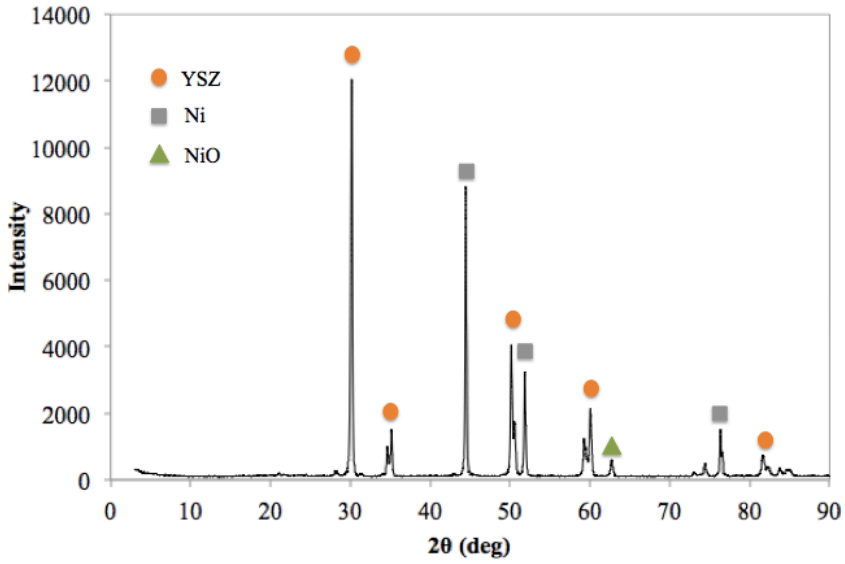

Figure 3.1. X-Ray Diffraction pattern of the conventional anode of an SOFC operated under H_2 fuel.

Together with the conventional cell peaks, XRD results of Mn impregnated cell shows the existence of different oxides of Mn that are produced after the operation of the cell (Figure 3.2). The additional peaks at unique 2θ values of 38° and 57° are appeared in the Mn impregnated cell and can be attributed to the presence of MnO_2 crystalline structure. Moreover, there are observable evidences that Mn_3O_4 is present according to the tiny peaks at 43° and 74° in the spectra based on the XRD database. Compared to the peaks of a conventional cell, Mn oxide peaks are much smaller in intensity in connection with the addition of Mn solution dropwise.

Accordingly, the formation of these oxides arrives at the conclusion of a slight decrease in porosity in anode part; on the other hand, the companionship of Mn oxides beside Ni may exhibit much lower rates of carbon deposition.

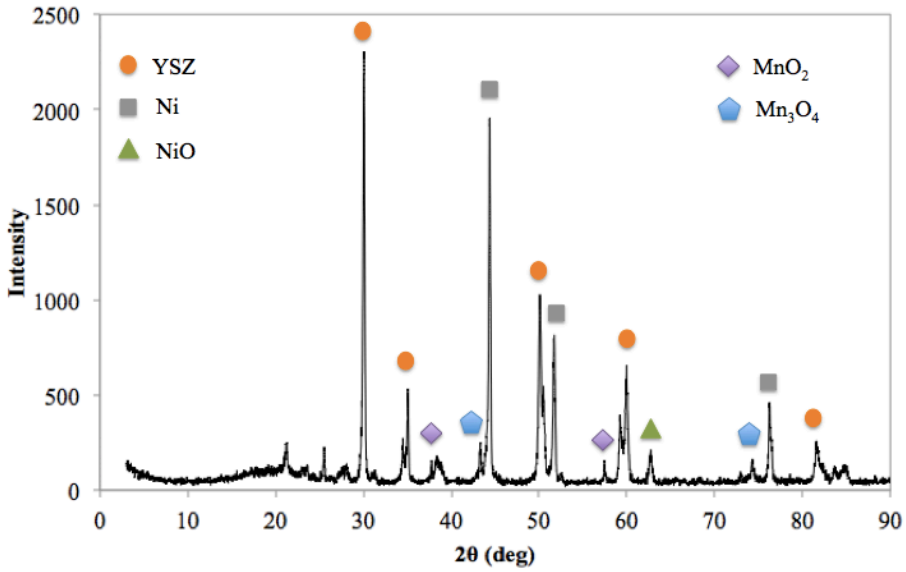

Figure 3.2. X-Ray Diffraction pattern of Mn impregnated anode operated under H_2 fuel.

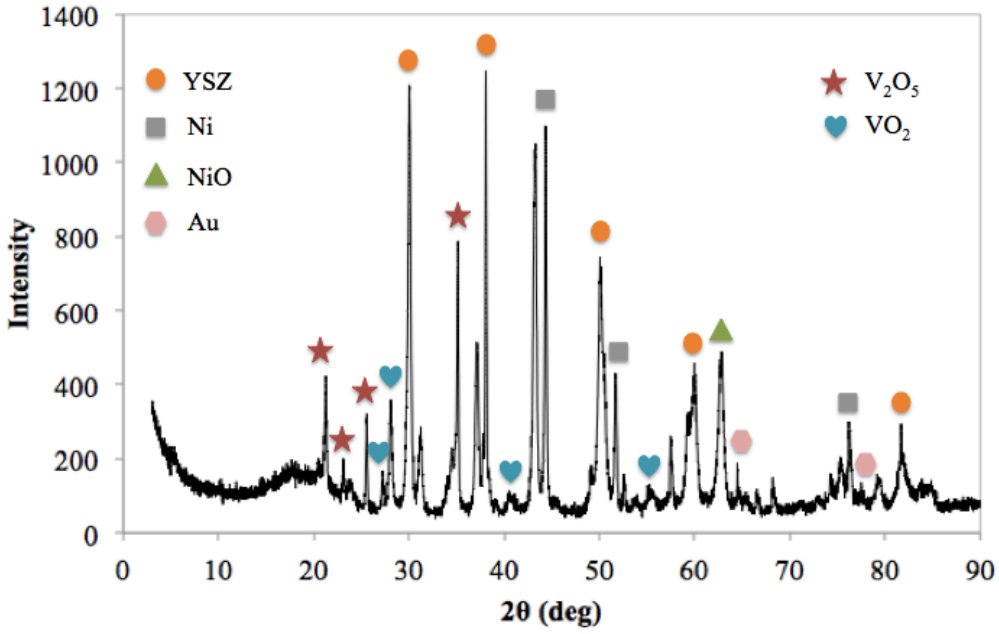

Figure 3.3. X-Ray Diffraction pattern of V impregnated anode operated under H_2 fuel.

After the operation of V impregnated conventional cell, acquired XRD result of the crystal structure is indicated in Figure 3.3. In common with Mn impregnation case, V impregnation resulted in two types of V oxide in the anode material. Along with the extraction of conventional anode peaks, remaining peaks at 27^o, 28^o, 42^o, 55.5^o are assigned to be of a V oxide that is VO_2 and the ones at 20^o, 22^o, 26^o, 35^o are for V_2O_5, while some other insignificant peaks at 64^o and 78^o are in the spectrum due to the presence of Au paste residuals on the surface of the analyzed anode part according to XRD database.

The reason why not Ni oxides but Mn and V oxides form after cell operation can be explained by experimentally observed electrode activities of anode materials, which is linked with the stability of surface-adsorbed atomic oxygen. According to a previously done research, the activity is highest in Ni case since it exhibits intermediate oxygen adsorption energy, while other transition metals have more tendencies to form oxides [41].

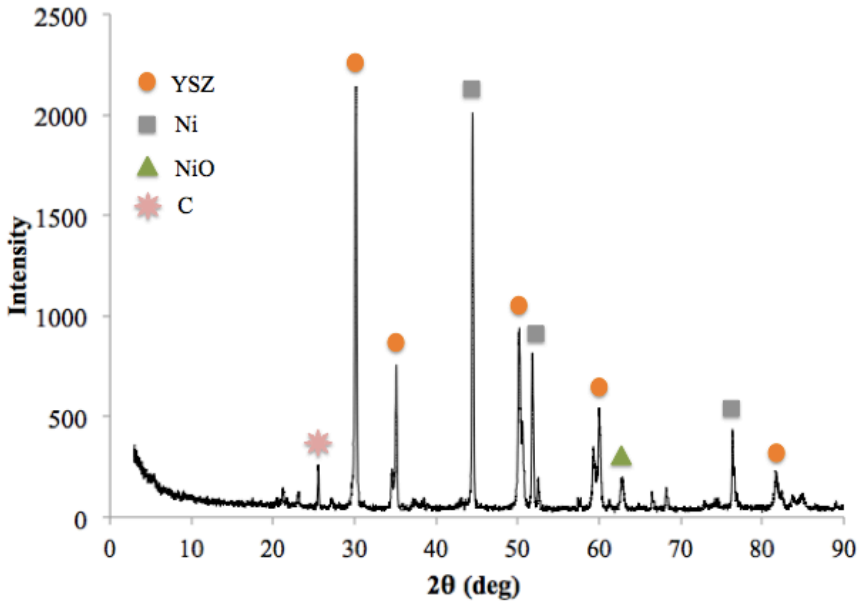

Figure 3.4. X-Ray Diffraction pattern of the conventional anode operated under CH_4 fuel.

In addition to the cells operated under H_2 fuel, XRD result of a conventional cell operated under CH_4 was illustrated in Figure 3.4. Apart from the conventional peaks of

NiYSZ fuel cell, there is a peak specific to the C and that can be attributed to C deposition on the anode surface.

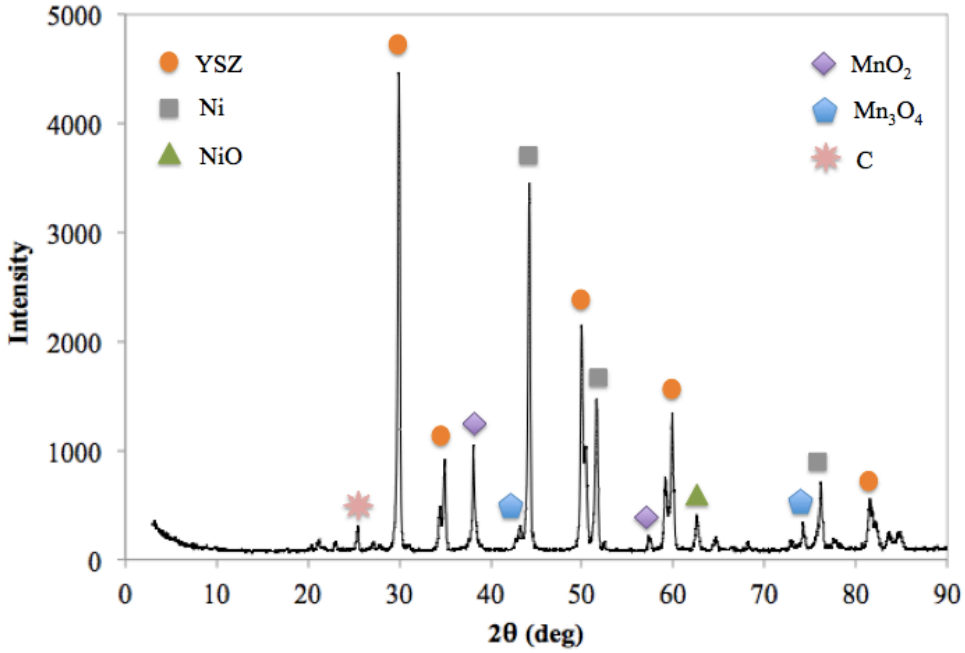

Figure 3.5. X-Ray Diffraction pattern of the Mn impregnated anode operated under CH_4 fuel.

XRD results of the Mn impregnated cell, which was operated under CH_4 fuel is also shown in Figure 3.5. The peak representing C deposition is at 26°, as it was in the conventional cell operated under CH_4 (Figure3.4).

3.2. X-Ray Photoelectron Spectroscopy (XPS) Results

For empirical formulas, elemental composition, electronic and chemical states of the elements, X-Ray photoelectron spectroscopy (XPS) is a technique that analyzes material with a beam of X-Rays and measures the number and kinetic energy of electrons emitted from the surface of anode [29]. In conjunction with its usefulness, XPS is also a leading analytical technique on account of its non-destructive habit; therefore, samples can be reused after analysis [42].

Following the knowledge about the precision of XPS analysis, it becomes indisputable that XPS is a pursuant way towards exploring the fuel cell materials extensively and having robust proves relating to the surface composition after impregnation.

The experiments were handled by using Thermo Scientific K-Alpha Surface Analysis instrument for all samples in this study and the survey spectrum of Mn impregnated cell is as shown in Figure 3.6.

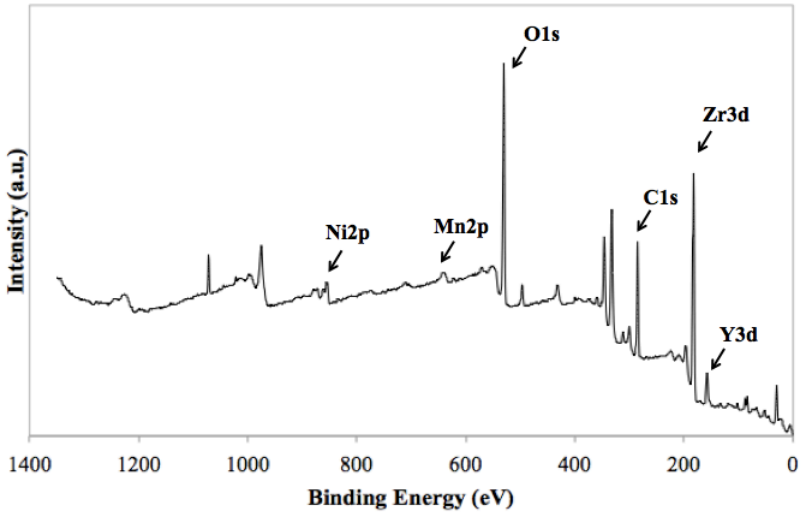

Figure 3.6. XPS survey analysis of Mn impregnated anode of an SOFC operated under H_2 fuel.

Alongside conventional peaks of Ni based anodes that are Ni, Zr, Y and O, a peak can be observed in the survey spectrum with the binding energy around 640 eV belonging to Mn. In order to have a deep understanding about the forms of Mn, Mn2p core level XP spectrum is plotted in Figure 3.7. The core level binding energies of $Mn2p_{1/2}$ and $Mn2p_{3/2}$ spectra for Mn_3O_4 are located at 653.38 and 640.08 eV, respectively, due to the mixed oxidation states of Mn atoms. The binding energy of $Mn2p_{1/2}$ line of MnO_2 is very close to $Mn2p_{1/2}$ line of Mn_3O_4 at 653.08 eV and since a relatively invisible peak represents both, it is difficult to detect and distinguish between them.

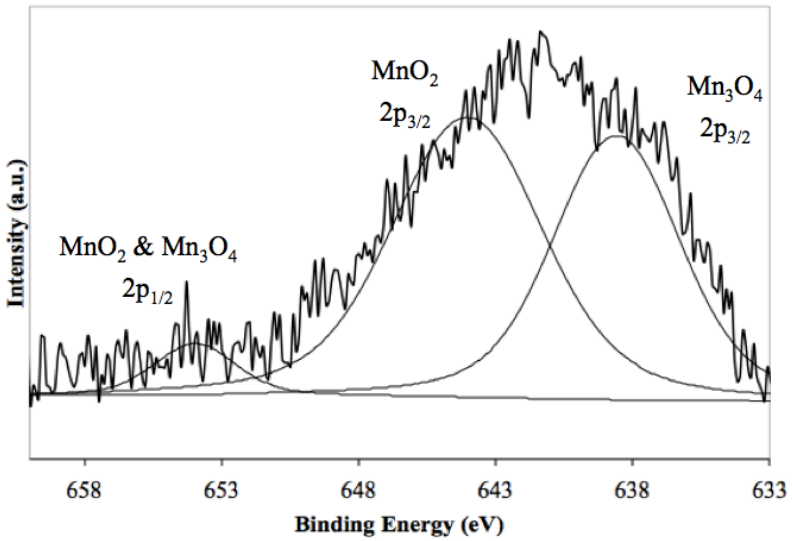

Figure 3.7. The Mn2p core level XP spectra of Mn Impregnated anode of an SOFC operated under H_2 fuel.

However, the peak exhibiting $Mn2p_{3/2}$ of MnO_2 is located at a different binding energy value, which is 643.78 eV. Therefore, the core-level spectra of Mn2p further ensure that the analyzed Mn impregnated sample consists of Mn^{2+}, Mn^{3+} and Mn^{4+} [43].

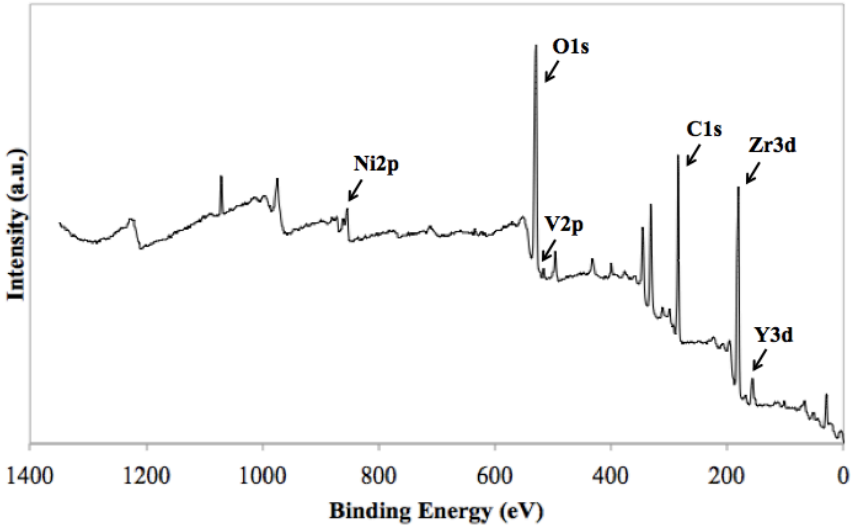

Figure 3.8. XPS survey analysis of V impregnated anode of an SOFC operated under H_2 fuel.

In Figure 3.8, the survey spectrum of V impregnated anode is shown and in addition to expected conventional peaks of anode material, a small peak around 520 eV can be observed. As it was in XRD results, small peaks representing Mn and V in survey spectrum of XPS results are because impregnation is performed with very low amounts of these transition metals.

The V2p core level X-Ray Photoelectron spectrum, as demonstrated in Figure 3.9, consists of a peak at 516 eV that can be attributed to $2p_{3/2}$ of VO_2. The binding energies of $2p_{1/2}$ and $2p_{3/2}$ spectra of V_2O_5 are located at 523 and 516 eV respectively, which is in agreement with XRD results [44,45]. Therefore, the core-level spectra of V2p further ensure that the analyzed V impregnated sample consists of V^{4+}, and V^{5+}.

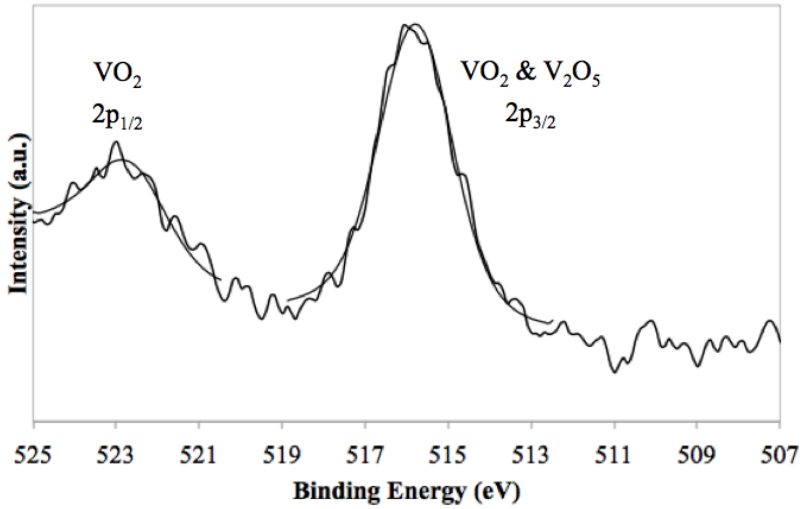

Figure 3.9. The V2p core level XP spectra of V Impregnated anode of an SOFC operated under H_2 fuel.

As it was mentioned before, Mn and V oxides form while Ni remains to be a metal after operation is because Ni is at an equilibrium point regarding the stability of surface-adsorbed atomic oxygen, whereas the other transition metals, in principle, are not [41].

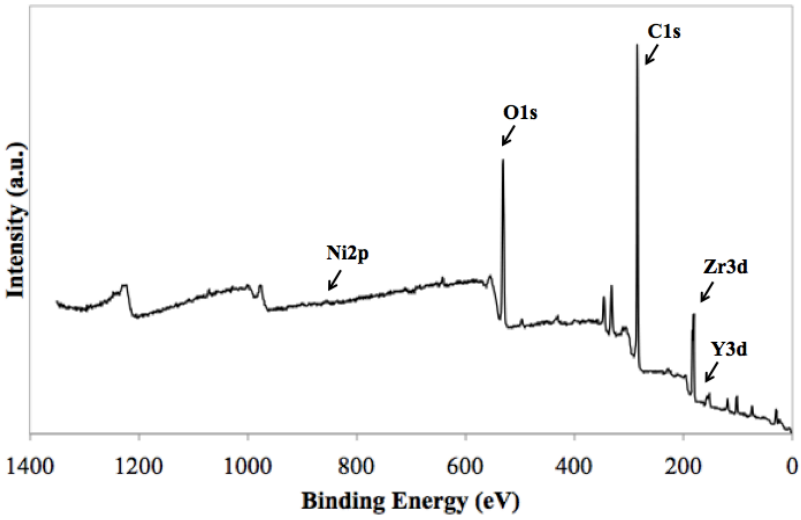

Figure 3.10. XPS survey analysis of conventional anode of an SOFC operated under CH_4 fuel.

In the XPS result of the conventional cell operated under CH_4, no Mn peak could be seen and a considerable increase in C1s peak intensity is observed (Figure 3.10). However, the Mn impregnated one operated with the same CH_4 fuel showed lower C1s peak intensity (Figure 3.11) that was a favorable result and confirmed the hypothesis of this study that Mn impregnation decreases C deposition on Ni anode.

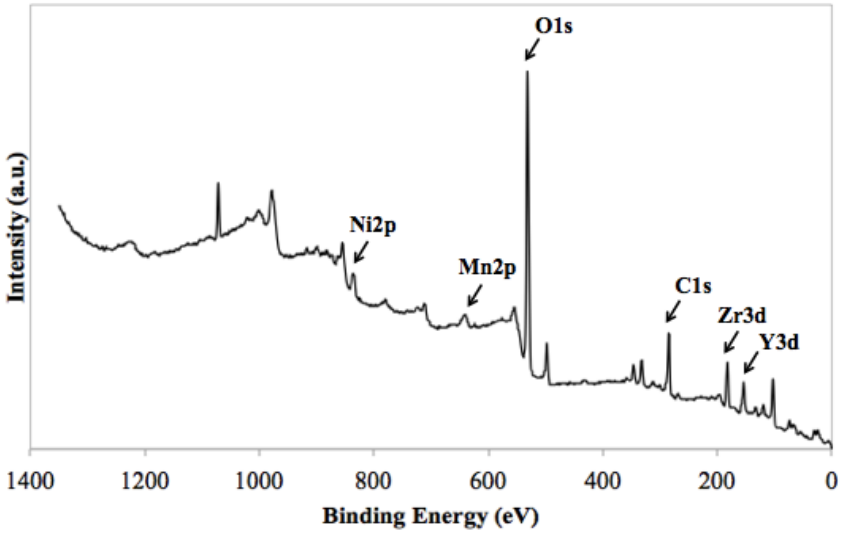

Figure 3.11. XPS survey analysis of Mn impregnated anode of an SOFC operated under CH_4 fuel.

3.3. Scanning Electron Microscopy (SEM) Results

Scanning electron Microscopy (SEM) enables images of a sample with elaborated high resolution allowing submicron scale by applying focused electron beams through the sample surface and reading secondary and backscattered electron signals. When electron beams hit the surface, secondary electron beams are released and read from the detectors immediately to supply an image based on the topography of the sample.

The most widely used detectors are Secondary Electron Detector (SED) collecting data depending on inelastic process and Backscattered Electron (BSE) Detector providing images arising from elastic scattering. As the backscattered electron yield is a function of atomic number, the acquired image from a BSE detector is determined by the weight of the atoms in the sample. In this study, Secondary Electron Imaging (SEI) is used by the aid of FEI-Phillips ESEM-FEG XL30 device at Boğaziçi University Advanced Technologies Research and Development Center.

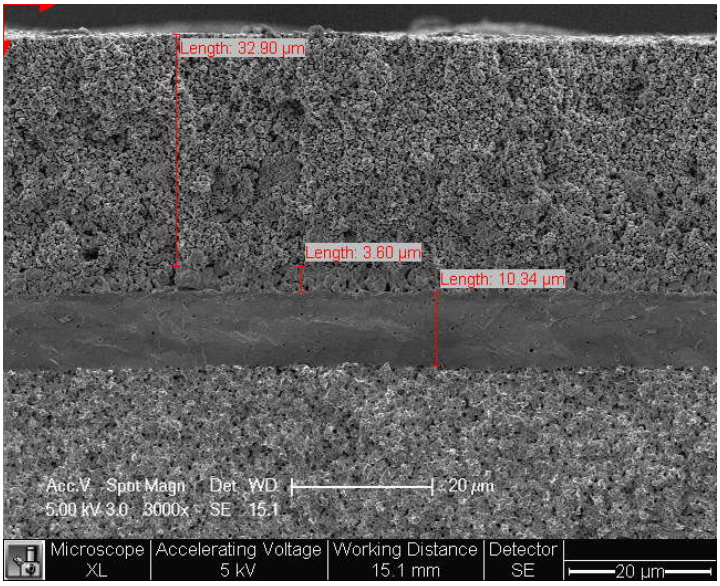

Figure 3.12. Cross-sectional SEM image of a conventional SOFC operated under H_2 fuel.

The image of a conventional SOFC cross section is shown in Figure 3.8. The layers are clear enough to be readily named as the porous cathode, dense electrolyte and porous anode from top to bottom respectively (Figure 3.12). Because the image is magnified and focused on a very small place in order to observe all the layers together with great extent of scope, not the whole anode layer but only a part of the anode can be seen from this picture; even though it is the thickest layer and the cell is an anode-supported cell.

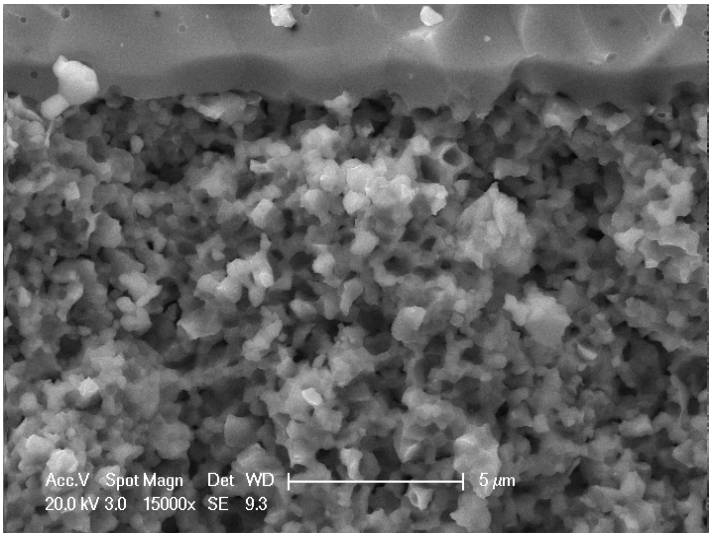

Figure 3.13. SEM image of the electrolyte and the anode of a conventional SOFC operated under H_2 fuel.

A closer look to the edge between electrolyte and anode is shown in Figure 3.13 where the dense pattern of the electrolyte and the porous structure of the anode can be observed. By comparison with the SEM image of Mn impregnated cell that is obtained with the same measurement criteria, it is distinguishable that the conventional one without Mn impregnation has more porous structure whereas the one with Mn impregnation is filled with Mn oxides after cell operation (Figure 3.14).

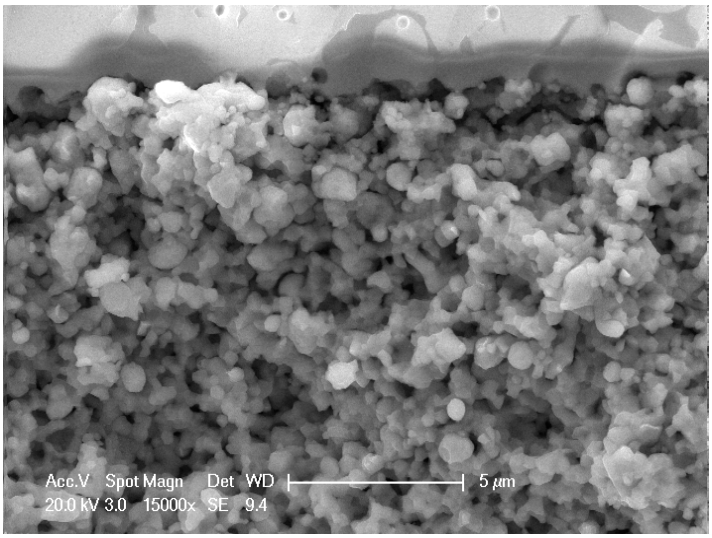

Figure 3.14. SEM image of the electrolyte and the anode of Mn impregnated SOFC operated under H_2 fuel.

Meantime inspecting topography, morphology, composition, and crystallographic information of specimens via SEM, very high magnifications are attainable without ever being fully extended. Another advantageous side of this type of analysis is that a good representation of the three dimensional sample can be derived. By benefiting from these advantages of SEM, zooming in Mn impregnated anode image opened a new door into better investigation. In Figure 3.15, the picture of bunch of particles is thought to be the Mn oxides that are extra to the reference picture of non-impregnated anode in Figure 3.13.

As well as in the scanning electron micrographs of Mn impregnated cell, V impregnated cell also exemplifies an anode picture that is filled with V oxides in comparison with the conventional cell. However the slight contrast difference between the anode layer close to electrode and the middle regions of anode material is because it is occasionally impossible to break the cell layers evenly before analyzing the lateral section (Figure 3.16).

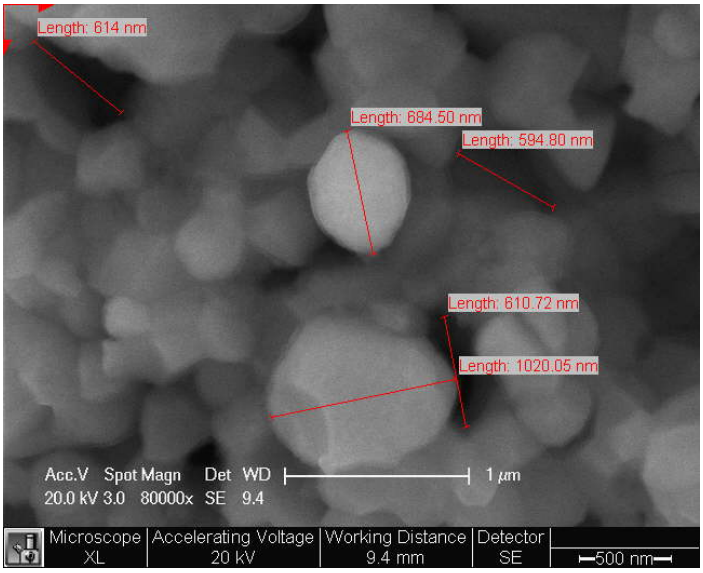

Figure 3.15. SEM image of the particles and cavities in Mn impregnated anode operated under H_2 fuel.

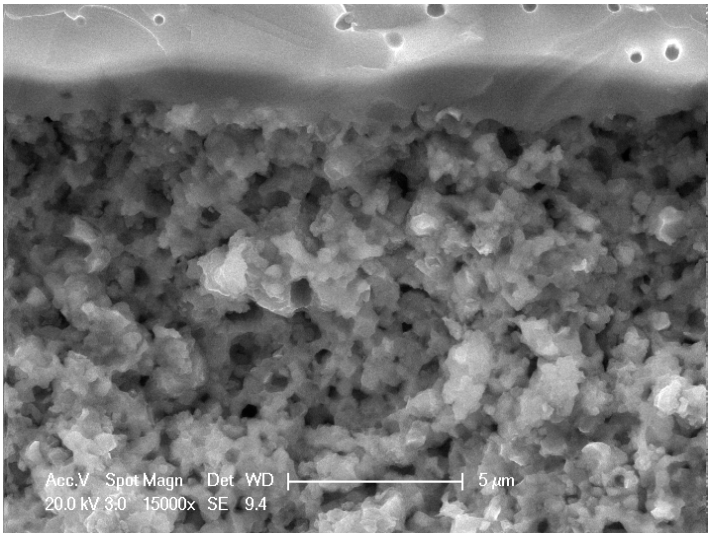

Figure 3.16. SEM image of the electrolyte and the anode of V impregnated SOFC operated under H_2 fuel.

For the inspection of particles and cavities of V impregnated sample, the anode material was photographed five times closer in Figure 3.17. Since in the first place V solution and after the operation V oxides are incorporated to the system, the volumes of cavities seem to be diminished to a minor extent. Furthermore, the particles that are in nanometer scale are assigned to be the oxides of V.

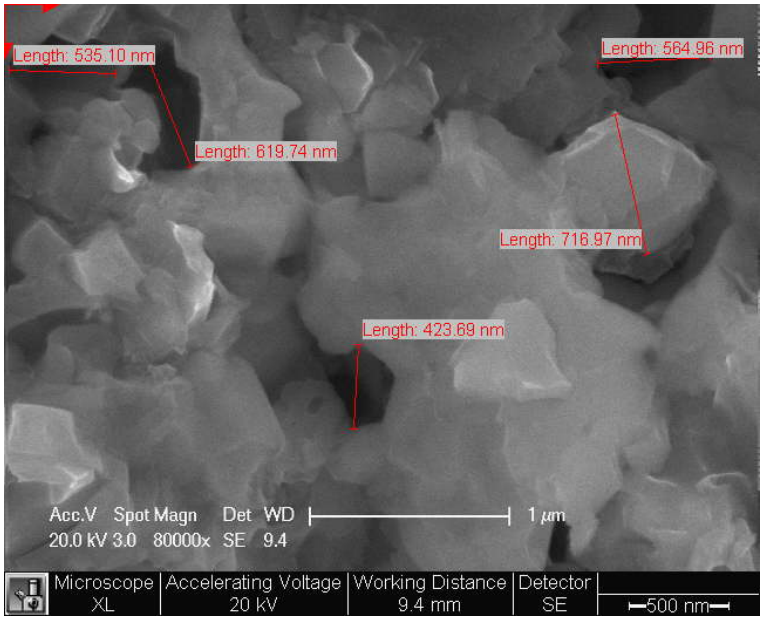

Figure 3.17. SEM image of the particles and cavities in V impregnated anode operated under H_2 fuel.

SEM analyses were done for the cells (both conventional and Mn impregnated) that were operated under CH_4 fuel, however there was no considerable difference in the pictures (Figure 3.18 and Figure 3.19) compared with the ones operated under H_2.

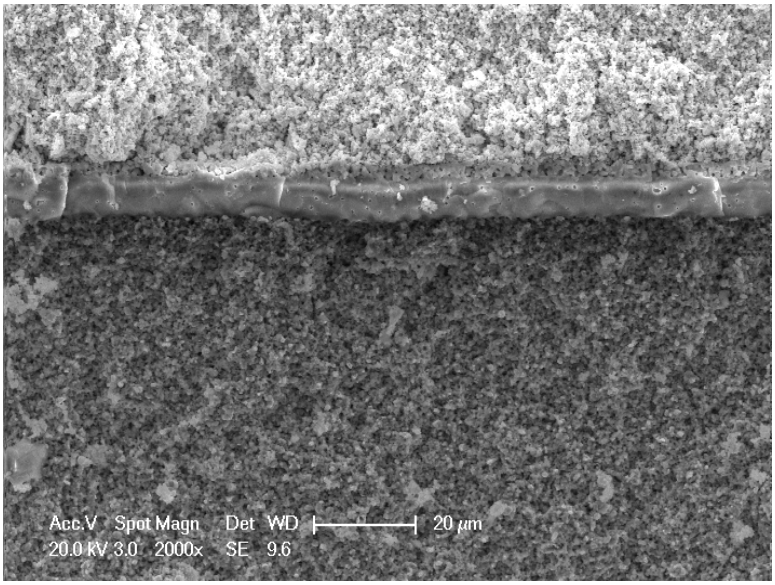

Figure 3.18. Cross-sectional SEM image of a conventional SOFC operated under CH_4 fuel.

In these SEM pictures of conventional (Figure 3.18) and Mn impregnated (Figure 3.19) cells cathode part is the one at the top, electrolyte is in the middle and anode is at the bottom.

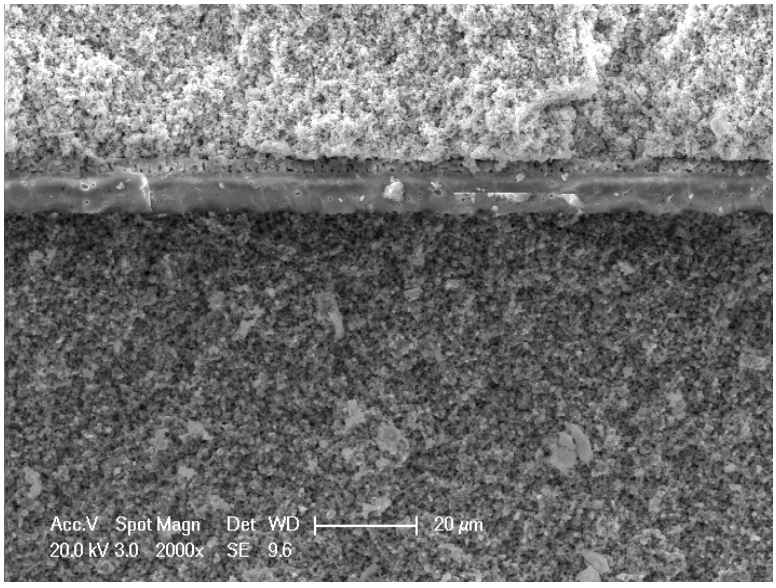

Figure 3.19. Cross-sectional SEM image of Mn impregnated anode of an SOFC operated under CH_4 fuel.

3.4. Linear Sweep Voltammetry (LSV) Results

As one of two types of electrochemical measurements performed in this study, Linear Sweep Voltammetry (LSV) tests were done by GAMRY Reference 3000 Potentiostat/Galvanostat. To examine the efficacy of electrochemical behavior of impregnation over conventional methods, polarization curves were determined using LSV at every 50°C starting from 400 °C to 800°C under 100 sccm (Standard Cubic Centimeters per Minute) H_2 as fuel and 20 sccm N_2 as carrier gas on anode side and air on cathode side. Also, CH_4 was set to be 32,60 sccm with the same amount of N_2, 20 sccm. The curves were arranged under a scan rate 20mVs^{-1} and in the potential range from -1,1 V to 0 V for both conventional and impregnated cells. By this means, LSV results can be employed for discovering the current-voltage (I-V) characteristics of cells through sweeping the voltage of the working electrode while measuring the current response.

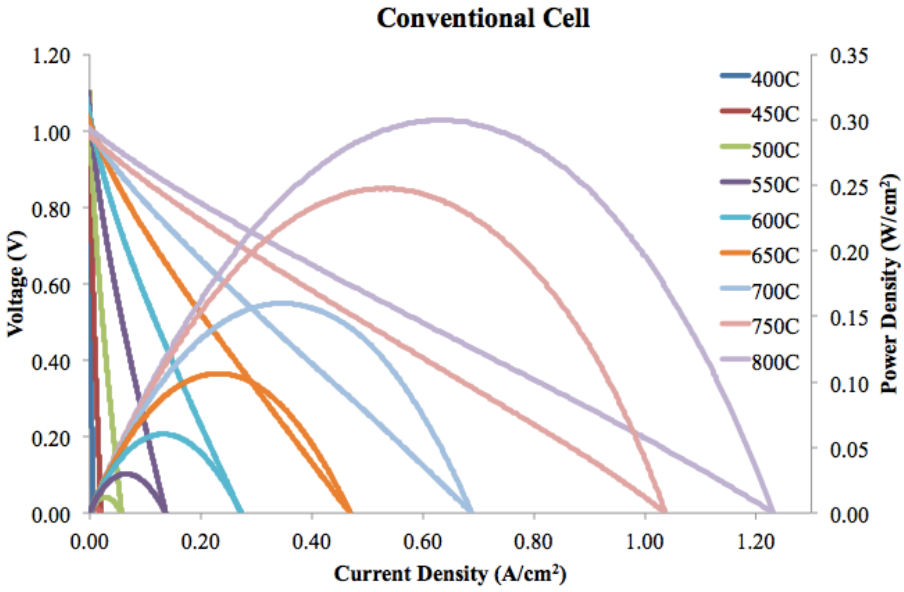

Figure 3.20. LSV results and power density values of the conventional cell at all temperatures operated under H_2 fuel.

As shown in Figure 3.20, I-V curves of conventional cell were plotted for each temperature and they were all collected in the same graph in order to perceive the tendency of the cell through increasing temperature. In addition, for the purpose of clarifying the influence of impregnation, power densities were calculated by multiplying the voltage and current values that are previously normalized based on the projected active areas (cm^2) of anode parts of the cells. Not surprisingly, measured current and calculated power increased gradually from 400°C to 800°C indicating that the performances of conventional cells enhance depending on the temperature they are operated.

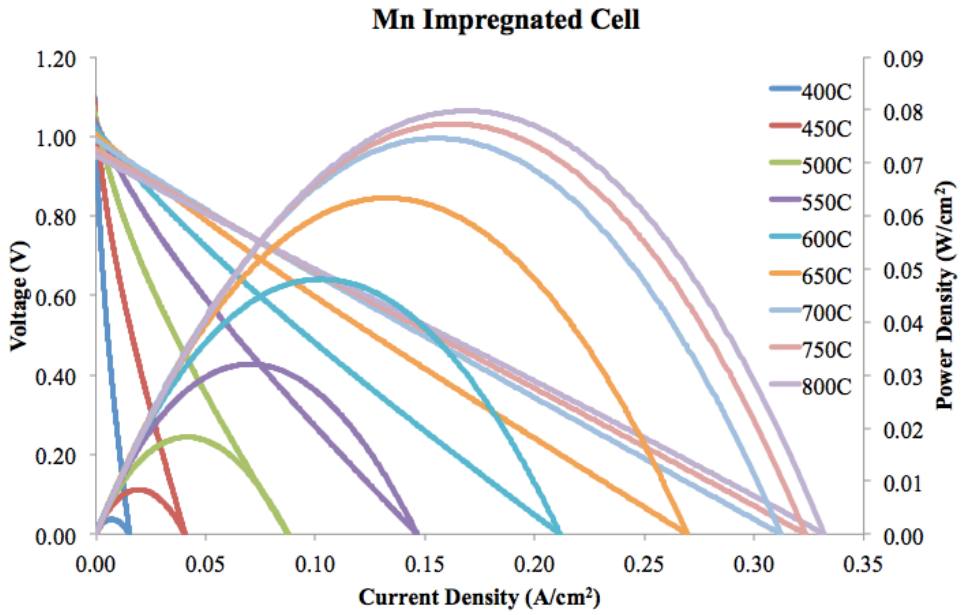

Figure 3.21. LSV results and power density values of Mn impregnated cell at all temperatures operated under H_2 fuel.

After testing the conventional cell, the system is cooled down to the room temperature and impregnation was performed on the anode side as it was explained in experimental part in detail. Mn impregnated cell whose results are shown in Figure 3.21, also came up with similar LSV results in which the order of I-V curves and power values displayed the same trend from starting point of 400 °C to the very end of 800°C.

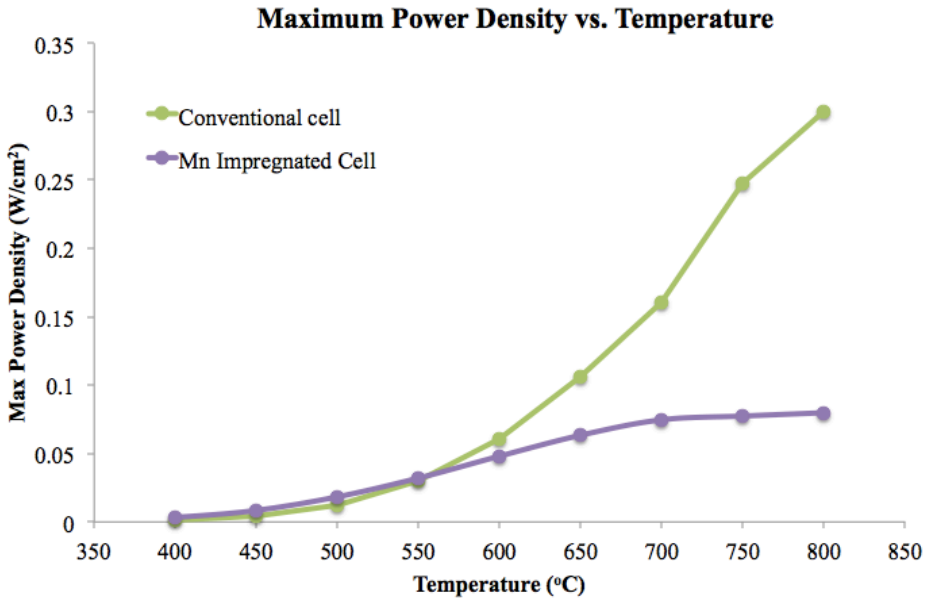

Figure 3.22. Maximum power density values (W/cm^2) for conventional cell and Mn impregnated cell operated under H_2 fuel.

The maximum power density values were plotted for each temperature of conventional and impregnated states of the cells and all of them were placed in the same graphs for the purpose of a comparison. When the maximum power density values of conventional and Mn impregnated cells are individually observed, it is once again seen that performance increases with increasing temperature. However more importantly, the performance of Mn impregnated cell exceeds the conventional cell between 400°C and 550°C whereas conventional cell has better capacities between 600°C and 800°C (Figure 3.22). Based on these results, it is quite obvious that Mn enables an anode compartment with better performances at intermediate temperature; yet, Ni is still a good choice for the temperatures higher than 600 °C since it can remain as metal and not be oxidized at temperatures higher than 600 °C [46].

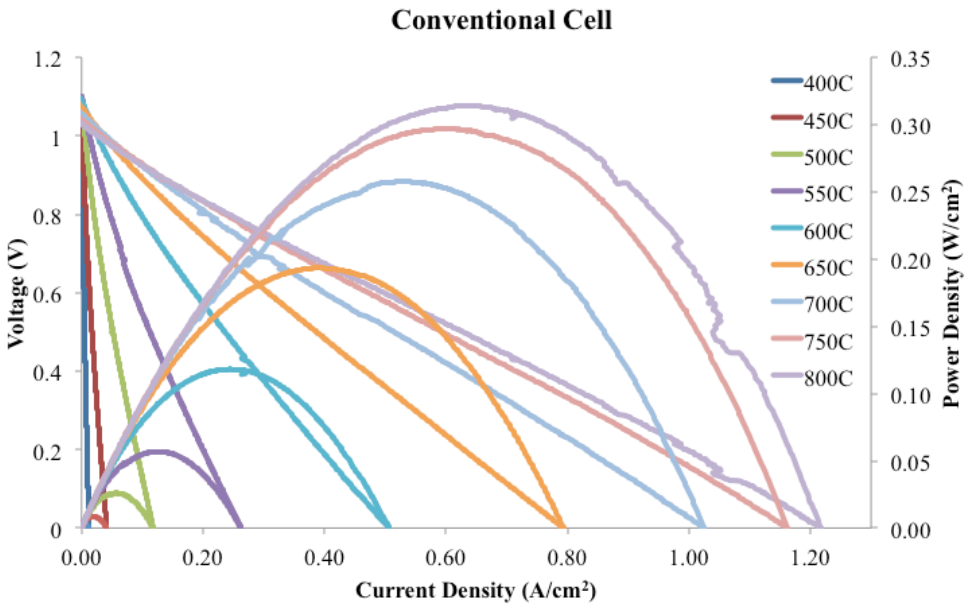

Figure 3.23. LSV results and power density values of the conventional cell at all temperatures operated under H_2 fuel.

The V impregnated conventional cell was analyzed with the same scan rate and scan range parameters of LSV measurement program so that the effects of impregnation could be clearly distinguishable. Both the conventional (Figure 3.23) and the V impregnated cells (Figure 3.24) states of the same cell exhibited increasing incremental current values with increasing temperature suggesting that there was no any imbalanced or unexpected situation concerning the cell set-up. Power densities were calculated for every single data point by multiplying the voltage and current density values specific to the calculated active area of anode.

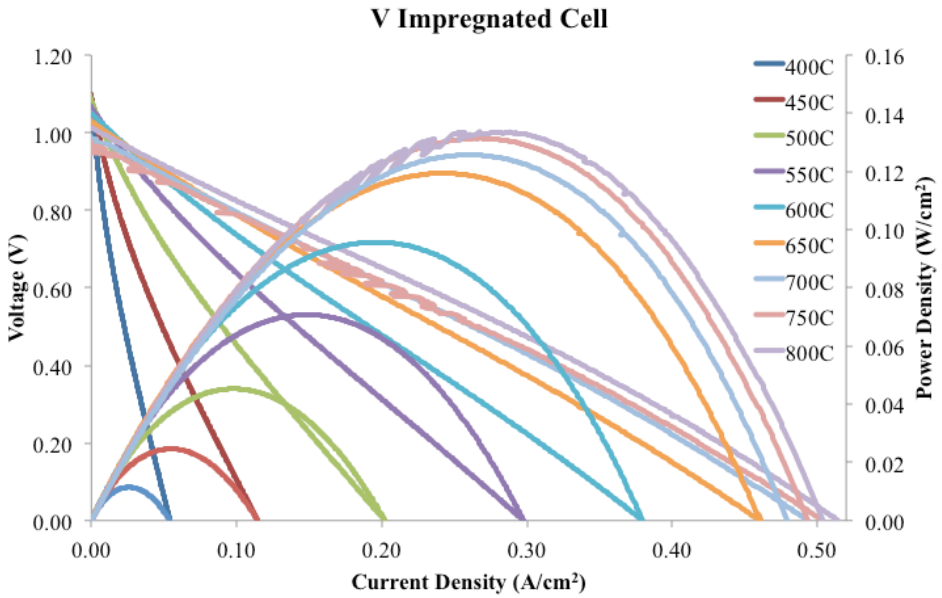

Figure 3.24. LSV results and power density values of V impregnated cell at all temperatures operated under H_2 fuel.

Secondly, the maximum power density values were decided for each operation temperature and plotted in one graph for both conventional and V impregnated states of the same cell (Figure 3.25).

After examining the graph in Figure 3.25, it is loud and clear that V impregnation has the same influence on the conventional cell as Mn impregnation. There are a number of numerical differences regarding the efficiency but the trend is showing that V impregnated cell has higher maximum power densities between 400^{o}C and 550^{o}C whereas conventional cell possesses preferable performance over V impregnated state between 600^{o}C and 800^{o}C. Being founded on the fact that there is a breaking point between 550^{o}C and 600^{o}C, it can be concluded that V empowers the anode compartment at intermediate temperature range as Ni remains as the anode material with highest capacity at temperatures higher than 600^{o}C. This is because Ni has oxidation states 2+, 3+ and can resist forming oxides at high temperatures unlike other transition metals [46].

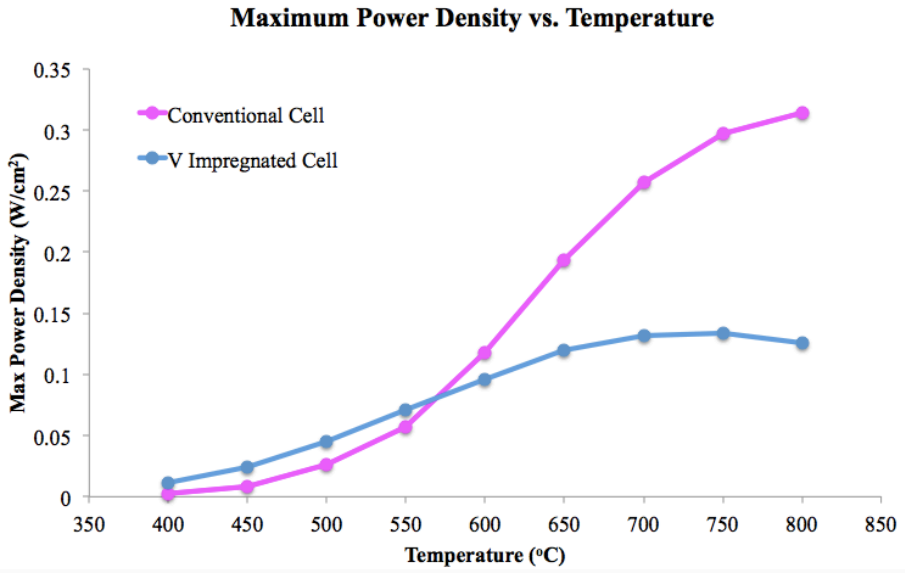

Figure 3.25. Maximum power density values (W/cm^2) for conventional cell and V impregnated cell operated under H_2 fuel.

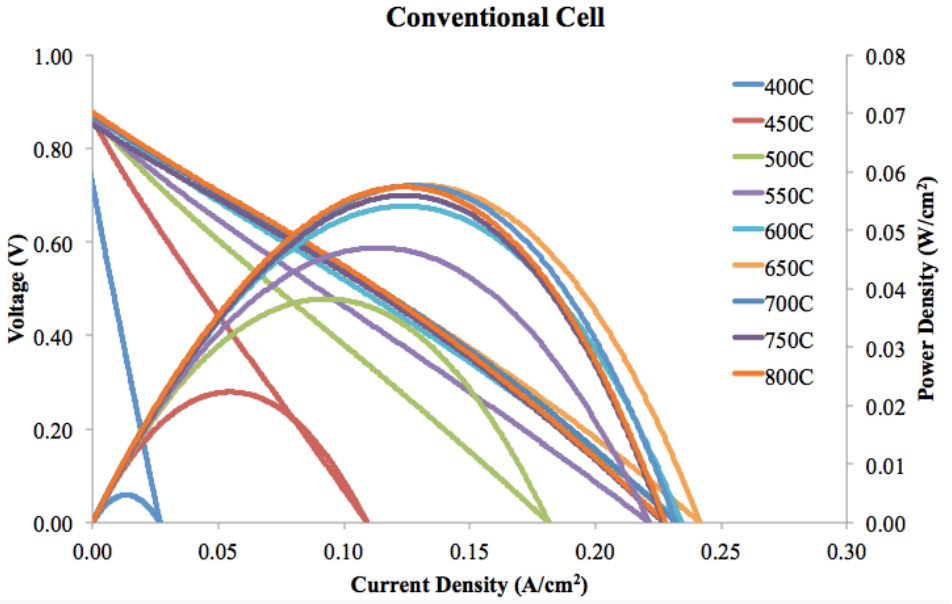

Figure 3.26. LSV results and power density values of the conventional cell at all temperatures operated under CH_4 fuel.

LSV results and power density values of the conventional cell that was operated under CH_4 fuel is shown in Figure 3.26. Current density and thus calculated power density values were close to zero meaning conventional cell did not work at all. Without impregnation, CH_4 spoiled the anode; C deposition blocked the anode surface that is a result, which is in agreement with the characterization tests. On the other hand, as for the Mn impregnated cell (Figure 3.27), current density and calculated power density values were much more promising and lead to the conclusion that Mn impregnation prevented C deposition considerably.

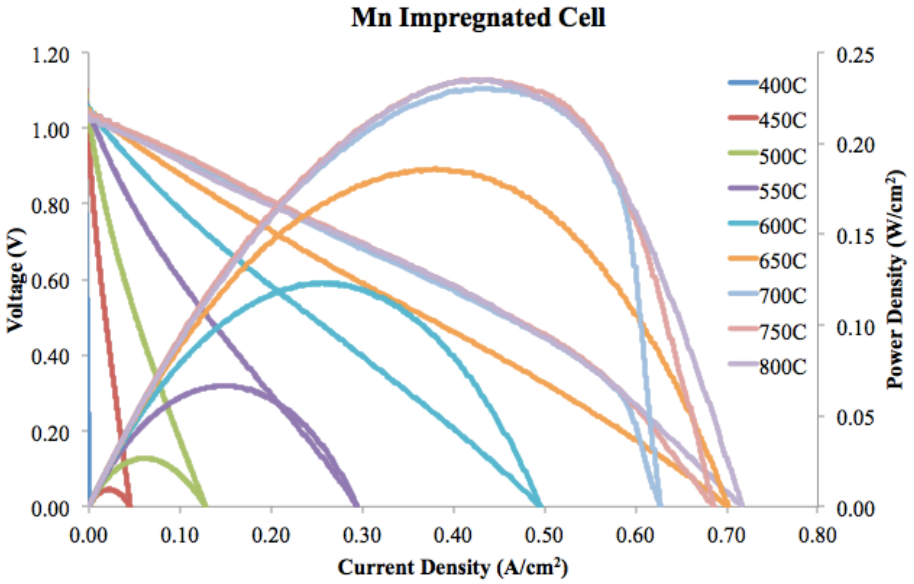

Figure 3.27. LSV results and power density values of the Mn impregnated cell at all temperatures operated under CH_4 fuel.

To evaluate different fuels impregnated cells, Mn impregnated cells were operated under H_2 and CH_4. The maximum power density values versus temperature graph were plotted for H_2 and CH_4 cases for Mn impregnated cells (Figure 3.28). It was concluded that CH_4 was able to show better performances than H_2 except 800°C where the fuel supply could not be efficient and another reason could be more carbon deposition at 800°C.

Maximum power density values for Mn impregnated cells operated under H_2 and CH_4 fuels in Figure 3.29 and maximum power density values for conventional and Mn impregnated cells operated under CH_4 fuel in Figure 3.30 are plotted. These two graph show that CH_4 is spoiling Ni performance compared to H_2 and Mn impregnation can be proposed as a solution to that problem.

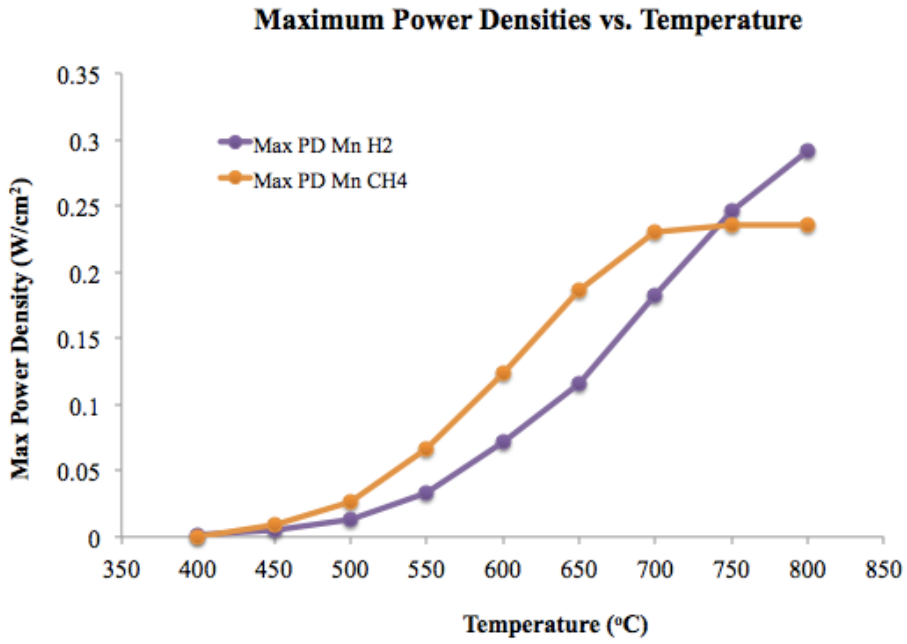

Figure 3.28. Maximum power density values (W/cm^2) for Mn impregnated cells operated under H_2 and CH_4 fuels.

Since Mn has several oxidation states, it also has the capacity to hold oxygen. These oxygens then could attract the C deposited on Ni surface forming CO_2 that can have the ability to liberate the anode surface.

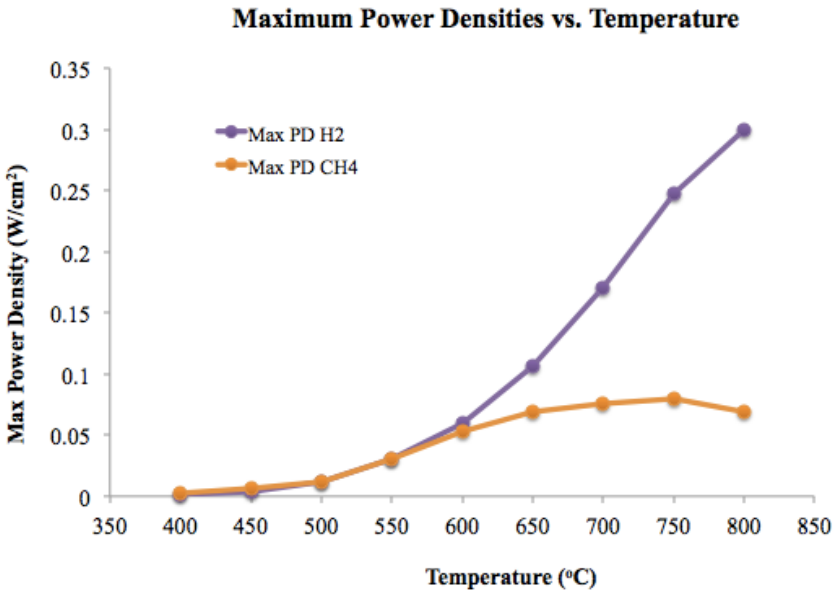

Figure 3.29. Maximum power density values (W/cm^2) for conventional cells operated under H_2 and CH_4 fuels.

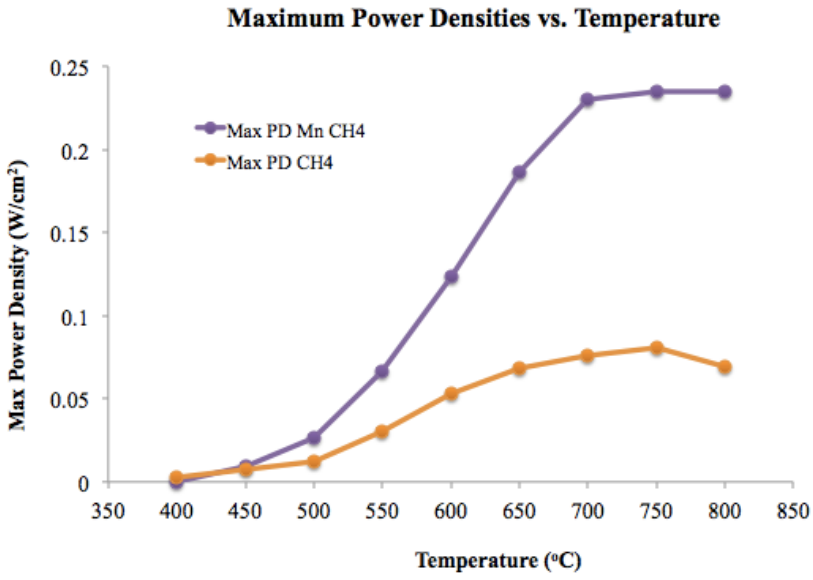

Figure 3.30. Maximum power density values (W/cm^2) for conventional and Mn impregnated cells operated under CH_4 fuel.

3.5. Electrochemical Impedance Spectroscopy (EIS) Results

The measure of the capacity of a circuit to resist the electrical current flow is called as impedance and it contains more complex elements and more complex behavior in circuits than resistance. Thus, a better definition for impedance could be made as the resistance that is dependent to the frequency (resistor, capacitor, inductor, etc.). Apart from that, Electrochemical Impedance Spectroscopy (EIS) measurements are done by collecting the response of the system to a small sinusoidal perturbation and by the computation of impedance at each frequency [47].

According to the discoveries made in this study, it can generally be stated that the results of Linear Sweep Voltammetry (LSV) are in accordance with the results of Electrochemical Impedance Spectroscopy (EIS) for conventional, Mn impregnated and V impregnated fuel cell samples. Yet, all data and fitting parameters are deeply investigated under this very title for further discussion. EIS has been successfully employed to this study of fuel cells by using AC and attaining small perturbations without considerably disturbing the measured properties, which are not viable through DC.

The experiments were conducted with the help of GAMRY Reference 3000 Potentiostat/Galvanostat device. Each impedance spectrum was measured in the frequency range from 100 000 Hz to 0.1 Hz under the excitation of a sinusoidal wave of 20mV amplitude. The impedance data were analyzed with Gamry EChem Analyst impedance analysis software and fitted to the proper equivalent circuit.

All electrochemical impedance curves of experimental and fitted data are chosen to be according to open circuit voltage (OCV). By this way, the scope of the investigation towards reactions could be maximized and all of the reactions taking place in the system could be surveyed in more detail.

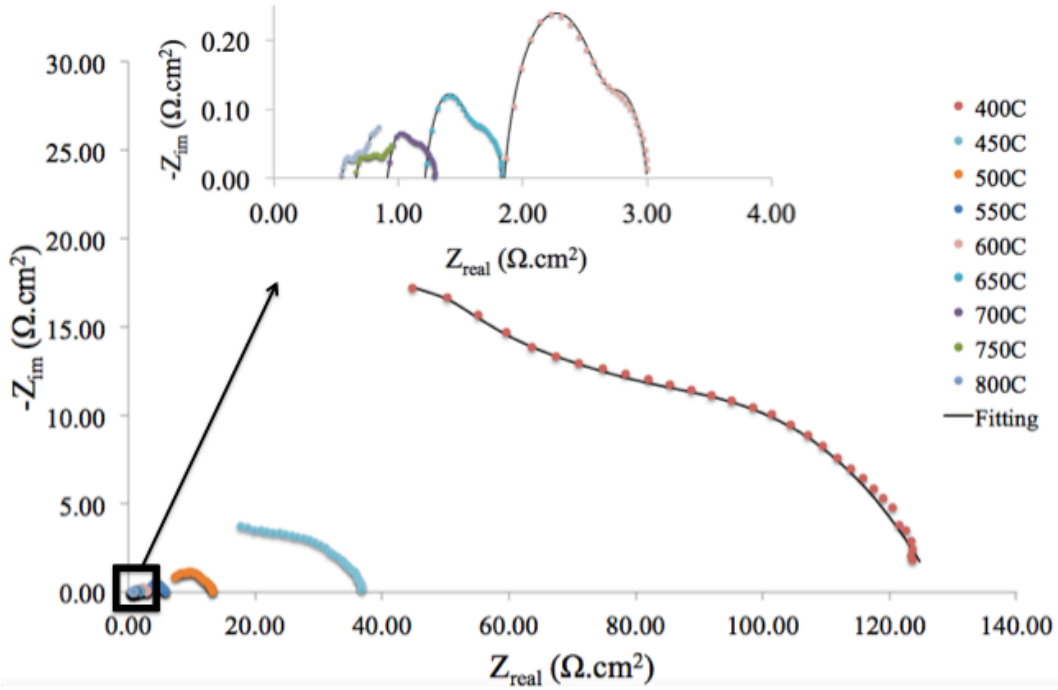

Figure 3.31. Experimental and fit Nyquist plots for conventional cell before Mn impregnation operated under H_2.

To start with, the experimental and fitted data of conventional cell are shown in Figure 3.31 and it is clear that the impedance values decrease depending on increasing temperature as anticipated. For electrolyte and cathode, the circuit elements were assigned by considering impedance curves; moreover, especially the curves for anode were investigated in depth and an extensive model was proposed. Finally, the equivalent circuit that was estimated based upon the curves and predicted reactions in order to fit EIS data is also illustrated in Figure 3.35.

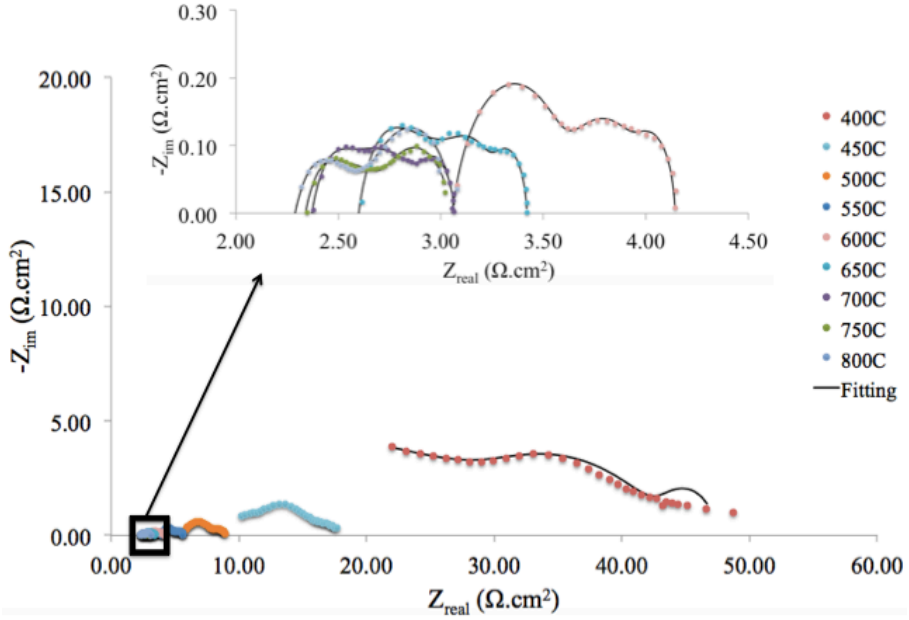

Figure 3.32. Experimental and fit Nyquist plots for Mn impregnated cell operated under H_2.

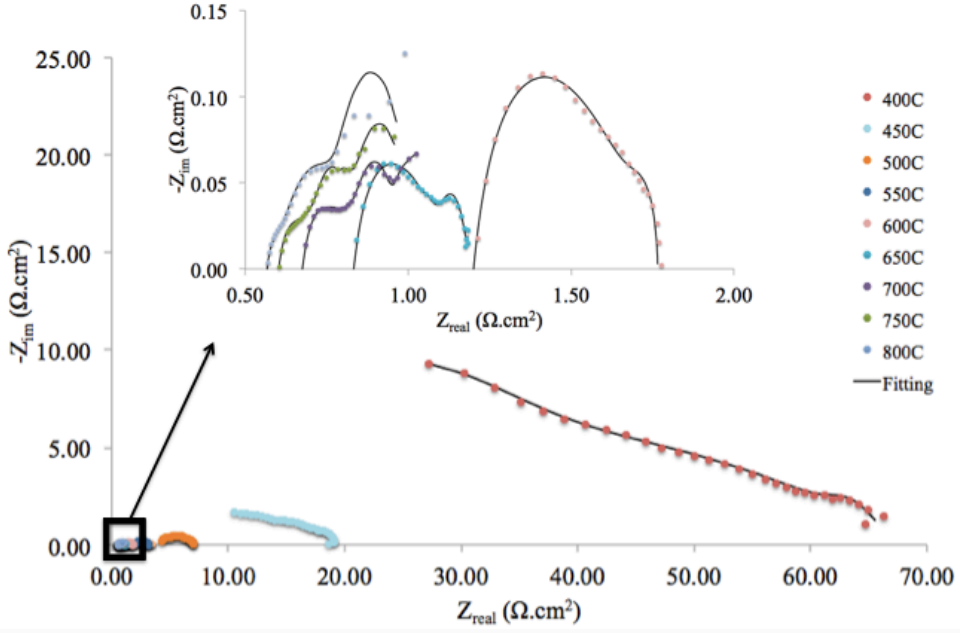

Figure 3.33. Experimental and fit Nyquist plots for conventional cell before V impregnation operated under H_2.

Data fitting for the conventional cell to be V impregnated was also done via Gamry EChem Analyst impedance analysis software according to the proposed equivalent circuit model. As a proper sign of the regularity of the system, impedance values decreased with an order with increasing temperature (Figure 3.33).

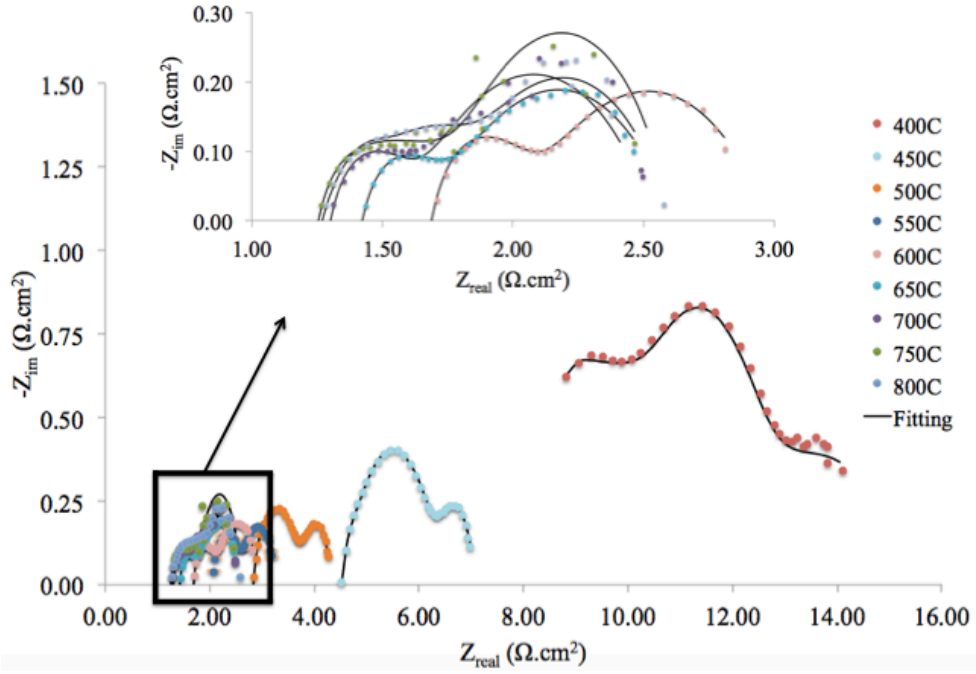

Figure 3.34. Experimental and fit Nyquist plots for V impregnated cell operated under H_2.

In the case of Mn (Figure 3.32) and V (Figure 3.34) impregnated samples, the same equivalent circuit (Figure 3.35) was used and the data of all analyzed temperatures were fitted accordingly.

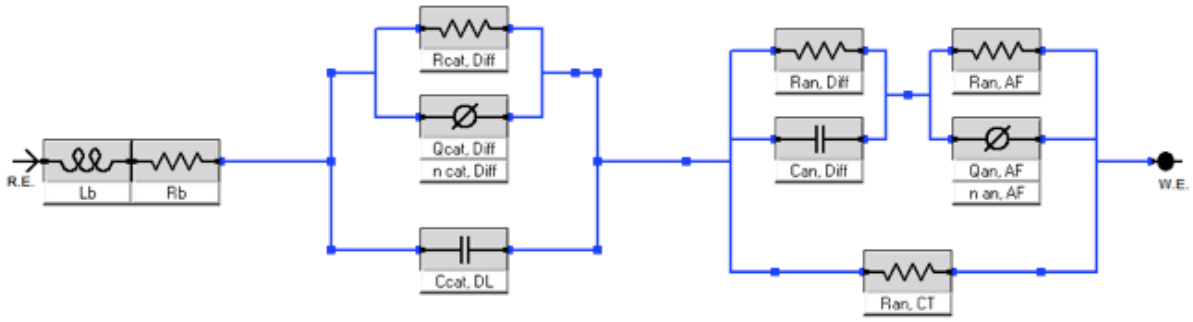

Figure 3.35. Equivalent circuit used to fit the electrochemical impedances.

In the proposed equivalent circuit, the inductance, abbreviated as L_b and the bulk resistance, R_b, are in series and associated to the connection of wires and YSZ electrolyte, respectively.

The cathode related circuit elements are resistance of the diffusion in cathode, R_{cat}, Diff, and the constant phase element (CPE), Q_{cat} Diff that are connected in parallel in themselves and also parallel to the cathode double layer capacitance C_{cat}, DL that stands for the reduction of oxygen on cathode (Figure 3.35).

For the anode process, there is a resistance representing the high frequency side of the curves in other words the anode charge transfer, R_{an}, CT and that is parallel to two parallel RQ elements connected in series to each other. The first RQ is linked with anode diffusion process consisting of R_{an}, Diff, and the capacitance of diffusion, C_{an}, Diff. The second RQ unit is thought to be the activation step containing the resistance of activation of fuels R_{an}, AF, and the constant phase element, Q_{an}, AF (Figure 3.35). The parameters concerning the electrolyte and cathode are postulated as constant for the entire polarization range and the differences in anode related processes were examined.

Table 3.1. The fitting parameters as a function of temperature for Conventional and Mn impregnated state of the cells operated under H_2 fuel

	T (^oC)	400	500	550	600	700	800
Conventional Cell	*Lb (H)*	$6.46x10^{-7}$	$0.31x10^{-7}$	$3.11x10^{-7}$	$3.68x10^{-7}$	$3.98x10^{-7}$	$4.01x10^{-7}$
	Rb ($\Omega.cm^2$)	10.6	2.57	2.54	1.64	0.74	0.47
	Rcat, Diff($\Omega.cm^2$)	14.70	2.55	1.03	0.711	0.127	0.071
	Ran, AF ($\Omega.cm^2$)	$8.97x10^2$	$1.03x10^2$	24.4	6.58	2.32	1.95
	Ran, Diff ($\Omega.cm^2$)	$10.2x10^2$	29.3	26.4	17.0	0.831	0.402
	Ran, CT ($\Omega.cm^2$)	$3.40x10^2$	30.7	3.15	1.30	0.793	0.633
Mn Impregnated Cell	*Lb (H)*	$1.65x10^{-8}$	$4.09x10^{-7}$	$3.97x10^{-7}$	$4.63x10^{-7}$	$4.84x10^{-7}$	$4.06x10^{-7}$
	Rb ($\Omega.cm^2$)	8.26	2.13	2.07	1.74	0.799	0.60
	Rcat, Diff($\Omega.cm^2$)	9.00	2.122	0.934	0.966	0.400	0.393
	Ran, AF ($\Omega.cm^2$)	98.3	33.6	7.27	7.09	2.52	2.06
	Ran, Diff ($\Omega.cm^2$)	72.7	29.2	27.9	20.2	5.86	3.34
	Ran, CT ($\Omega.cm^2$)	29.5	6.27	1.40	1.37	0.840	0.755

The proposed equivalent circuit (Figure 3.35) was fitted to the impedance curves for all types of cells investigated and all data taken from the fitting step were tabulated including L_b, R_b, R_{cat}, Diff, R_{an}, AF, R_{an}, Diff, and R_{an}, CT. The inductance, L_b, is related to the connection of wires in the system, it stays almost constant and is out of consideration while increasing the temperature in conventional cell itself and while also enquiring the effects of impregnation.

Besides that, the resistance of electrolyte reduces with rising temperature for conventional cell since the rising temperature increases the ionic conductivity and cathode diffusion resistance values were close to each other showing no considerable difference regarding conventional and Mn impregnated states. Because impregnation aimed anode parts not cathodes (Table 3.1).

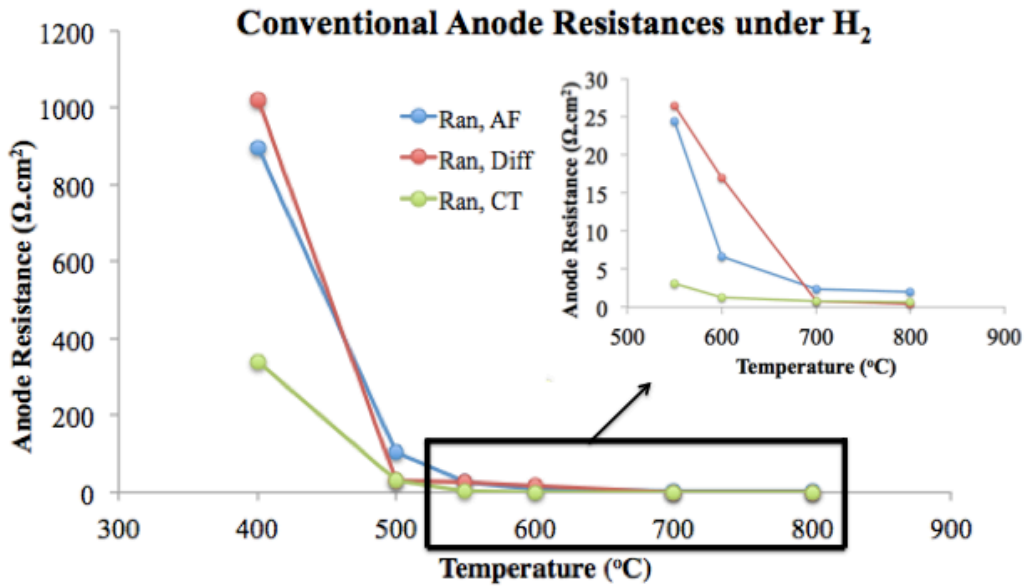

Figure 3.36. Resistances of activation of fuels, diffusion and charge transfer steps versus temperature graph of the conventional cell before Mn impregnation operated under H_2 fuel.

As far as the resistances of the anode part are concerned, the data for anode was plotted against temperature variable in order to see the fluctuation of the parameters inclusively. According to the lines in the plot, resistances of impregnated cell are lower and it is possible to say that there is a common trend for all resistances since they are decreasing with increasing temperature (Figure 3.36). However, the all types of resistances do not exhibit the same values for the same temperatures. At the first temperature, 400^{o}C, where the analysis started, the diffusion resistance is highest for conventional cell while the resistance of the activation of fuels is the second since there is a catalyst to accelerate this step and finally the charge transfer resistance of anode is the easiest reaction type among all (Figure 3.36).

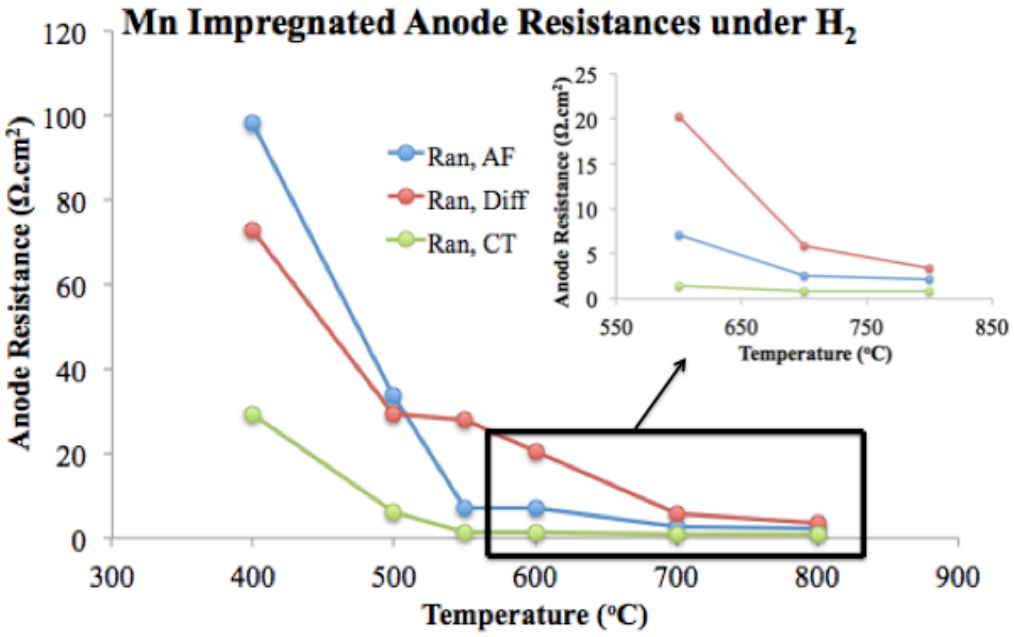

Figure 3.37. Resistances of activation of fuels, diffusion and charge transfer steps versus temperature graph of the Mn impregnated cell operated under H_2.

The Mn impregnated state of the cell shown in Figure 3.37 had different resistance values than the conventional one (Figure 3.36) as expected. The activation of fuels was the hardest reaction type that could be resulted from the fact that the Mn together with conventional catalyst, Ni, was activated and worked well at higher than 450°C. Not surprisingly, the diffusion of species stayed more resistive compared to charge transfer step. Yet, there was a decrease for all types of reactions in the Mn impregnated case.

Specific to the R_b parameter, Mn impregnation decreased R_b values, since the formation of oxides in the anode contributed to the overall ionic conductivity of the cell.

Table 3.2. The fitting parameters as a function of temperature for Conventional and V impregnated states of the cells operated under H_2 fuel.

	T (^oC)	400	500	550	600	700	800
Conventional Cell	*Lb (H)*	$4.60x10^{-7}$	$1.68x10^{-7}$	$3.52x10^{-7}$	$4.26x10^{-7}$	$4.39x10^{-7}$	$4.19x10^{-7}$
	Rb (Ω.cm²)	4.19	3.55	1.82	1.04	0.388	0.513
	Rcat, Diff(Ω.cm²)	16.27	2.55	1.57	1.50	1.35	0.180
	Ran, AF (Ω.cm²)	66.8	22.6	17.5	2.37	2.15	0.239
	Ran, Diff (*Ω.cm²*)	150.2	14.4	10.0	5.82	2.76	0.744
	Ran, CT (Ω.cm²)	15.0	4.23	1.32	0.982	0.841	0.607
V Impregnated Cell	*Lb (H)*	$4.00x10^{-7}$	$4.23x10^{-7}$	$4.44x10^{-7}$	$4.74x10^{-7}$	$4.76x10^{-7}$	$4.50x10^{-7}$
	Rb (Ω.cm²)	2.09	2.04	1.76	1.50	0.974	0.649
	Rcat, Diff(Ω.cm²)	21.9	2.844	1.23	1.20	1.31	0.140
	Ran, AF (Ω.cm²)	57.4	26.2	24.6	14.0	2.39	2.13
	Ran, Diff (*Ω.cm²*)	14.19	8.62	7.13	6.42	5.32	5.17
	Ran, CT (Ω.cm²)	11.4	2.29	1.28	1.26	1.25	1.18

The equivalent circuit in Figure 3.35 was also fitted for conventional and V impregnated states of the same cell and data were tabulated including L_b, R_b, R_{cat}, Diff, R_{an}, AF, R_{an}, Diff, and R_{an}, CT parameters. The inductance, L_b, value remained at around 10^{-7} range and R_b decreased with increasing temperature that is similar with conventional and Mn impregnated cells investigated before meaning that increasing temperature provides easier oxide ion

transformation process. There were no significant changes in R_{cat} values of conventional and V impregnated states.

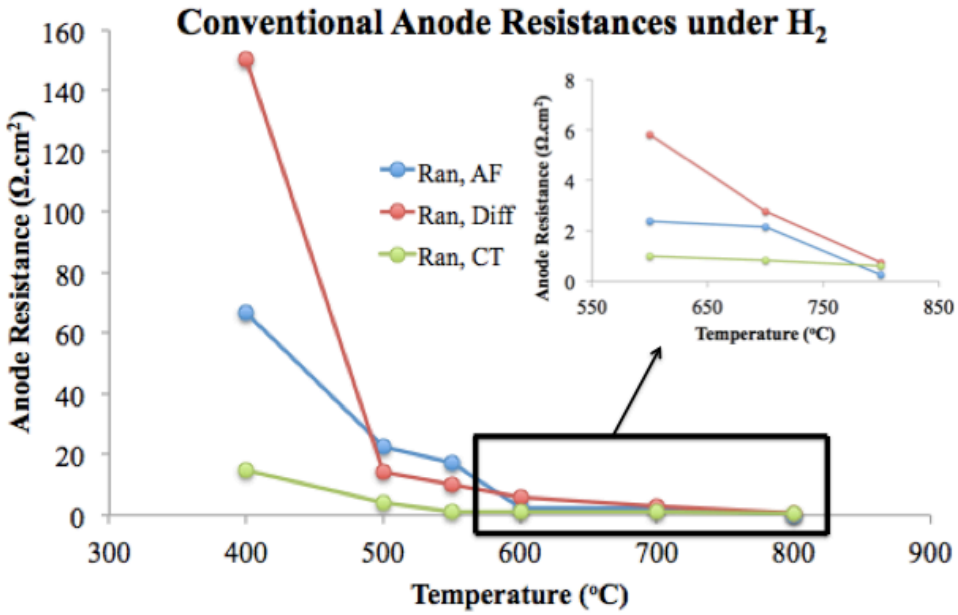

Figure 3.38. Resistances of activation of fuels, diffusion and charge transfer steps versus temperature graph of the conventional cell before V impregnation operated under H_2.

At the beginning of the analysis, the most resistive part was the diffusion in anode for conventional cell, since there is a catalyst for activation of fuels to fasten fuel activation and charge transfer is the easiest step among these three. This is why the resistances of activation of fuels and charge transfer followed the diffusion respectively (Figure 3.38).

In the V impregnated cell, activation of fuels exhibited as the most resistive part as it was in Mn impregnated case. It could be caused by the same reason that V with Ni were activated and worked more efficiently at temperatures higher than 450^{o}C as it worked as metal at that temperature region (Figure 3.39) [46].

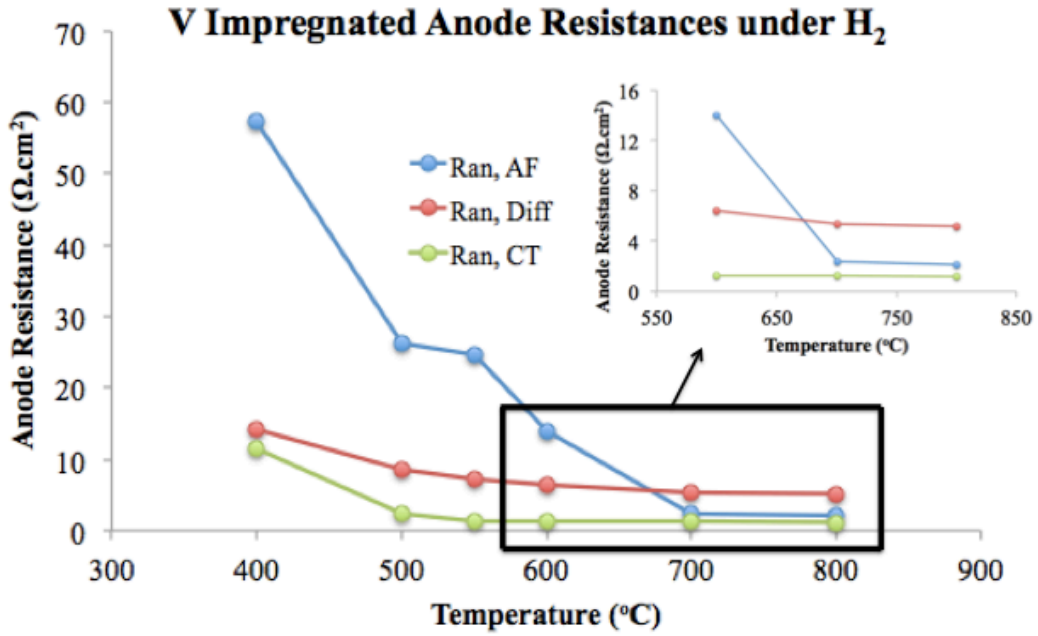

Figure 3.39. Resistances of activation of fuels, diffusion and charge transfer steps versus temperature graph of the conventional cell to the V impregnated cell operated under H_2.

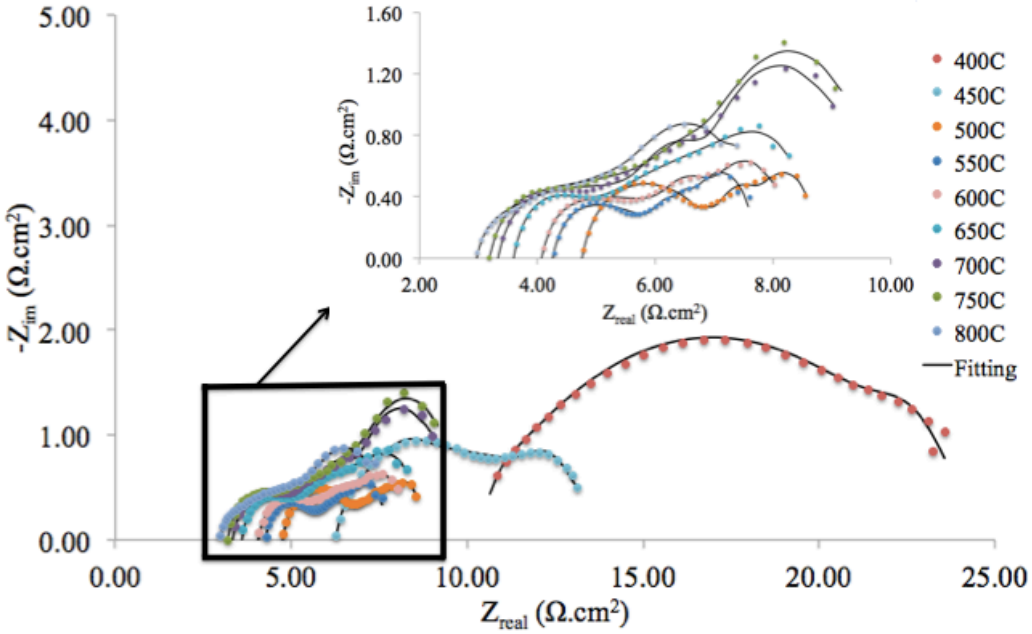

Figure 3.40. Experimental and fit Nyquist plots for conventional cell operated under CH_4.

The experimental and fitted data of conventional and Mn impregnated cell that were operated under CH_4 are shown in Figure 3.40 and Figure 3.41. The impedance values decrease depending on increasing temperature as expected. Finally, the same equivalent circuit that was proposed for the EIS curves of the cells operated under H_2 fuel was also used for the cells operated under CH_4 fuel meaning that all cell types went through the same electrochemical processes (Figure 3.35).

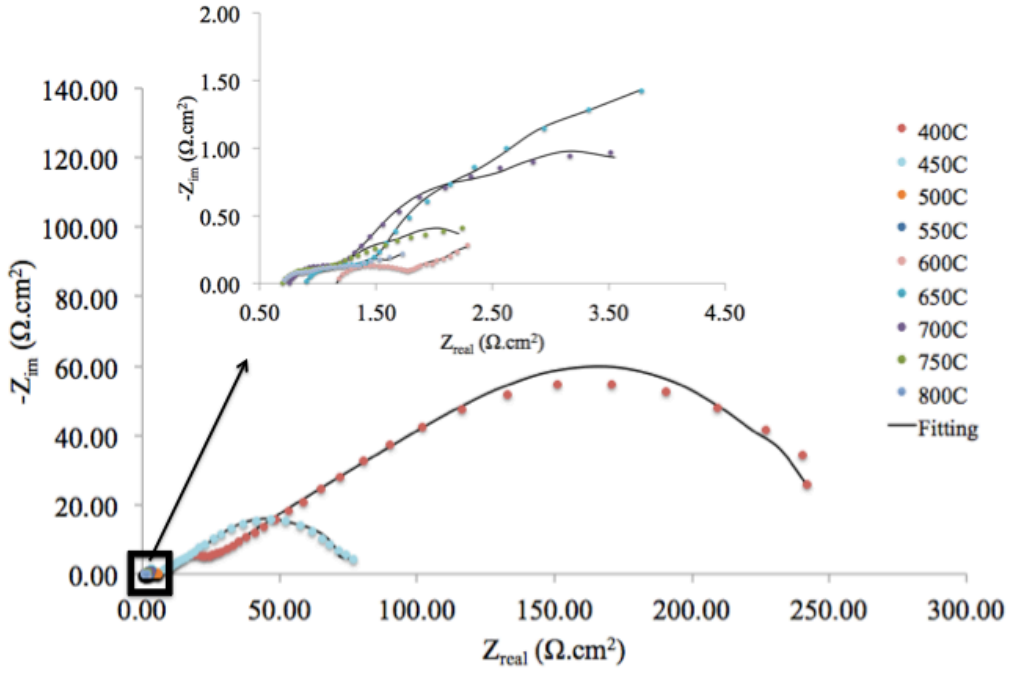

Figure 3.41. Experimental and fit Nyquist plots for Mn impregnated cell operated under CH_4.

Table 3.3. The fitting parameters as a function of temperature for Conventional and Mn impregnated states of the cells operated under CH_4 fuel.

	T (^oC)	400	500	550	600	700	800
Conventional Cell	*Lb (H)*	$8.38x10^{-7}$	$5.89x10^{-7}$	$6.73x10^{-7}$	$6.78x10^{-7}$	$6.19x10^{-7}$	$4.73x10^{-7}$
	Rb ($\Omega.cm^2$)	9.46	4.26	3.35	2.61	1.67	1.57
	Rcat, Diff($\Omega.cm^2$)	15.94	8.698	2.33	0.399	0.3	0.107
	Ran, AF ($\Omega.cm^2$)	25.7	8.76	3.84	2.33	1.75	1.22
	Ran, Diff ($\Omega.cm^2$)	34.1	16.4	15.9	6.10	3.46	2.42
	Ran, CT ($\Omega.cm^2$)	23.4	15.4	3.66	1.84	0.803	0.794
Mn Impregnated Cell	*Lb (H)*	$48.1x10^{-7}$	$6.10x10^{-7}$	$6.68x10^{-7}$	$1.71x10^{-7}$	$7.35x10^{-7}$	$7.06x10^{-7}$
	Rb ($\Omega.cm^2$)	25.41	3.603	2.391	1.569	0.918	0.742
	Rcat, Diff($\Omega.cm^2$)	8.457	2.057	1.246	1.361	0.667	0.167
	Ran, AF ($\Omega.cm^2$)	166.0	85.51	3.90	2.132	1.11	0.92
	Ran, Diff ($\Omega.cm^2$)	708.6	27.24	9.691	3.405	3.062	2.474
	Ran, CT ($\Omega.cm^2$)	99.3	53.29	4.55	1.541	0.84	0.724

The equivalent circuit in Figure 3.35 was fitted for conventional, Mn and V impregnated states of the cells in Table 3.1 and Table 3.2, respectively. The same equivalent circuit was also fitted for conventional and Mn impregnated cells that were operated under CH_4 fuel (Table 3.3). The data were tabulated including L_b, R_b, R_{cat}, Diff, R_{an}, AF, R_{an}, Diff, and R_{an}, CT parameters. The inductance, L_b, value remained at around 10^{-7} range and R_b

decreased with increasing temperature that is similar with the cells investigated before. R_{cat} values remained very close to each other under conventional and Mn impregnated conditions.

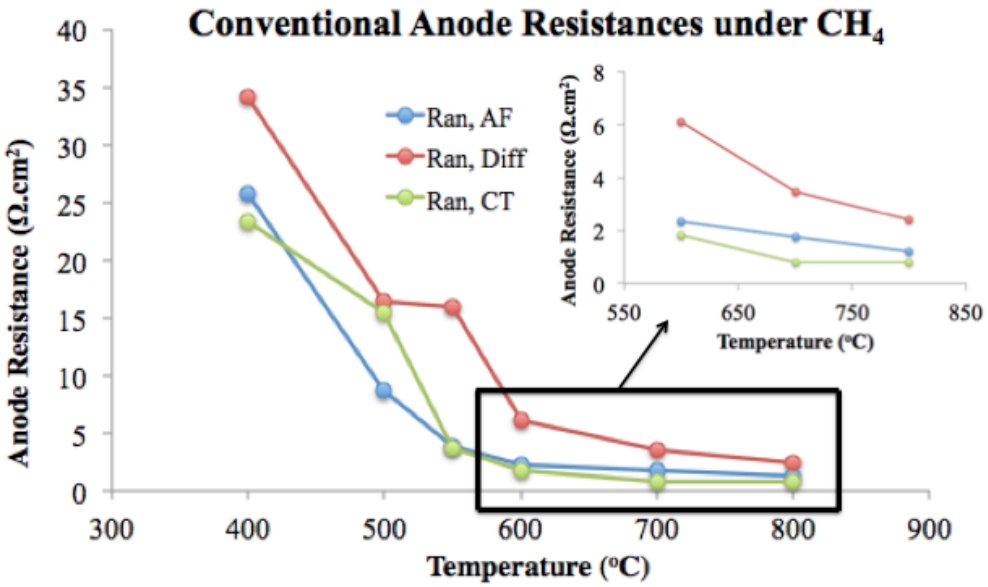

Figure 3.42. Resistances of activation of fuels, diffusion and charge transfer steps versus temperature graph of the conventional cell operated under CH_4 fuel.

In order to observe the difference in resistances of the anode; the resistances of activation of fuels, diffusion and charge transfer steps were plotted against temperature variable (Figure 3.42). As a general trend, resistances decreased with increasing temperature and diffusion of species seemed as the most resistive step; activation of fuels step with a catalyst is the second and charge transfer showed the lowest resistance values because moving electrons that are very small in volume was the easiest step.

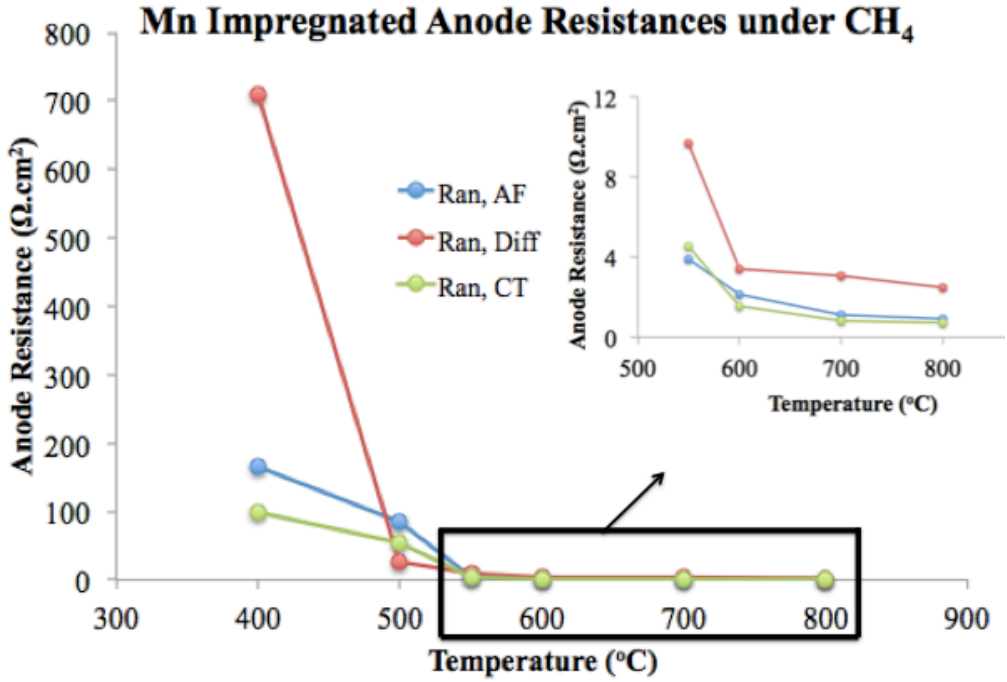

Figure 3.43. Resistances of activation of fuels, diffusion and charge transfer steps versus temperature graph of the Mn impregnated cell operated under CH_4 fuel.

For Mn impregnated cell operated under CH_4 fuel, all resistances of the anode were plotted (Figure 3.43) and a more detailed graph can also be seen for the temperatures between 550-800^oC in the same figure where the resistances decreased with increasing temperature.

Total anode resistances of conventional and Mn impregnated cells are plotted against temperature in Figure 3.44. As it is in agreement with previous results, regarding the cells operated under H_2 and CH_4, Mn impregnated ones exhibited lower resistances before 600^oC and higher resistance values thus worse performance can be observed between 600-800^oC for Mn impregnated cell. In Figure 3.45, the total anode resistances of conventional and V impregnated states of the cells are plotted. Before 600^oC, performances were very close at 550^oC and at lower temperatures V impregnation enabled the conventional cell with better performances while between 600-800^oC conventional cell had higher resistances and worse performances.

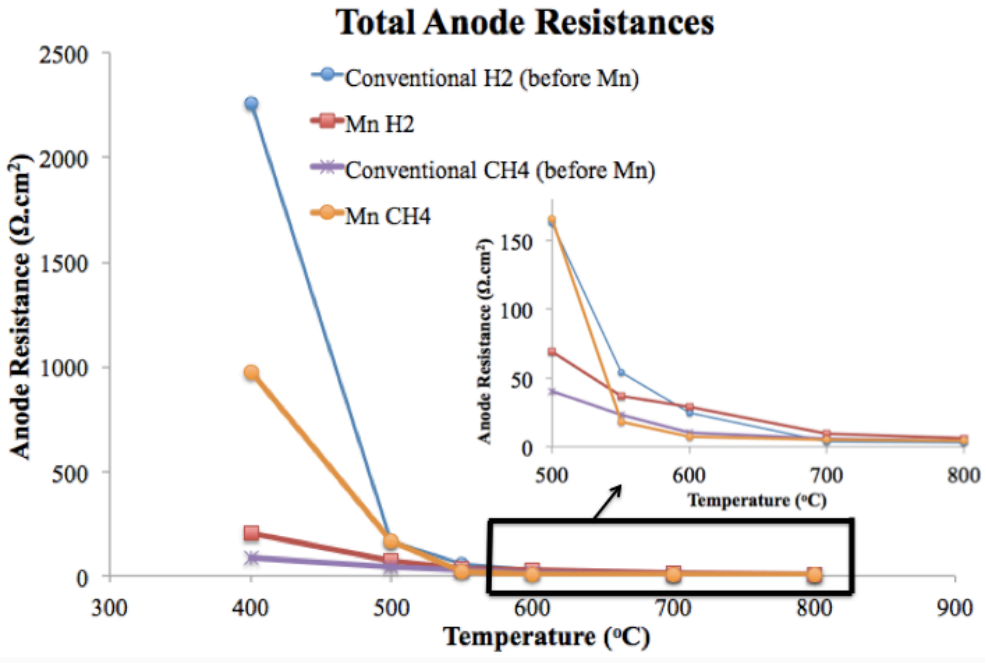

Figure 3.44. Total resistances of activation of fuels, diffusion and charge transfer steps versus temperature graph of conventional and Mn impregnated cells under H_2 and CH_4.

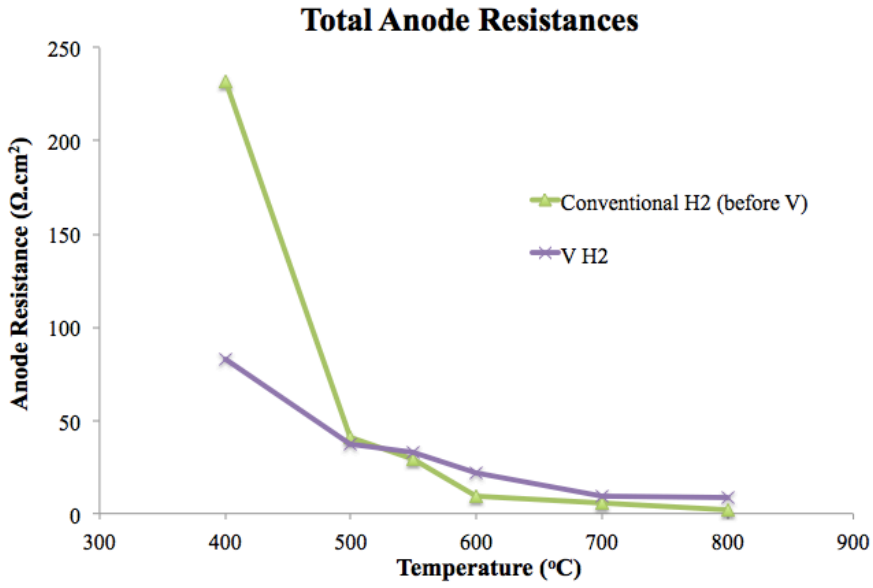

Figure 3.45. Total resistances of activation of fuels, diffusion and charge transfer steps versus temperature graph of conventional and V impregnated cells under H_2.

The reason why the sum of all resistance values is not equal to total resistance in data fitting graphs is that circuit is completed via the least resistive route and does not travel through all resistance elements proposed in the circuit.

4. CONCLUSION

Solid oxide fuel cells provide highly efficient electricity production with negligible pollution via a series of electrochemical reactions. That is why they have taken great interest due to the rapid growth in global energy demand in recent years. Based on this point of view, this thesis defines a form of explorative research in which SOFC concept is taken as the focal point on the whole and in particular enhancing the anode performance that contributes to the overall fuel cell performance is the ultimate purpose.

This rigorous study has been developed based on the idea of improving the performance of the conventional Ni based anodes via a very simple and practical technique that is named as wet impregnation. Since anode is the part of oxidation reactions, multivalent transition metals such as Mn and V are selected for impregnating the anode part. To be able to discover the differences brought by the wet impregnation of transition metals, conventional cells were fitted to the cell operation setup and performance experiments were done at each 50^{o}C from 400 to 800^{o}C under H_2 fuel. After that, for observing the Mn impregnation effects on the system, following the cooling procedure, this time Mn impregnated state of the same cell was operated at the same operation temperatures. As for V impregnation, the identical procedure was performed with H_2 as fuel. In addition, Mn impregnated cell was operated under CH_4 and the effects were observed. Because of the C deposition possibility on Ni anodes, impregnation with Mn could have the potential of providing the anode surface durability and better operation conditions concerning oxidation capacity.

During operations LSV and EIS performance tests were implemented and conventional and impregnated states of the cells were compared in themselves. Following the performance tests, each cell was taken off the cell operation setup and characterized by XRD, XPS and SEM to make sure whether the performance test results were in agreement with the information obtained from characterization techniques.

I-V curves and Nyquist plots proved the stability of the experimental setups since they demonstrated increasing performance with increasing operation temperature. For data analysis of Nyquist plots, an equivalent circuit was proposed and fitted to each type of the cell operated. The types of resistances were also proposed for the whole equivalent circuit; however, the main focus was on the anode resistances which are named as the resistance of diffusion of species, the resistance of activation of fuels and the resistance of charge transfer in anode compartment. As a general trend, these resistance values decreased with increasing temperature; yet, there was another trend followed by the system regarding the easiness of the reactions proposed. The diffusion exhibited the most resistive part since the transfer of the species in the material was the most difficult step. Secondly, the activation of fuels with a catalyst to fasten that part followed the diffusion and finally charge transfer step showed the lowest resistance values.

After harmonizing all data acquired from the steps explained above, it can be concluded that Mn and V impregnation enable solid oxide fuel cells with a better anode performance than Ni for the temperatures between 400-550^{o}C and Ni remains to be metal and thus a favorable candidate for temperatures higher than 600^{o}C. More importantly, Mn has affirmative effects regarding the cell efficiency and specifically eliminating the C deposition problem while operating the cells under CH_4 fuel.

Above all, the easiness and practicality of the method introduced to the conventional solid oxide fuel cell system was the most significant motive that made the results of this study more prospering and encouraging for further studies.

5. FUTURE WORK

This study is essentially based on the impregnation of two transition metals to the anode parts of SOFCs, and several characterization and performance tests were implemented to see the effects developed. This thesis could take on a task to be a key as creating curiosity for different transition metals, methods, and mechanisms, which at the end has the capacity for opening the doors for further discoveries concerning deeper analysis towards improving SOFCs.

It could be interesting to continue with other transition metals such as titanium and using different characterization techniques would provide much better understanding as well. The way the setup is constructed could also be changed in order to minimize possible cracks in the system at high temperatures.

Most importantly, while producing electricity via transition metal impregnated SOFCs, taking advantage of other hydrocarbon fuels such as propane, butane and syngas without giving rise to instabilities to the cell setup would be an enormous step by eliminating the carbon deposition problem of conventional Ni based anode systems. By this way, the principal advantage of SOFCs over other fuel cells, which is the potential of utilizing all types of fuels indiscriminately, could be brought into action.

REFERENCES

1. Procter, P., *Cambridge International Dictionary of English*, Cambridge University Press, 1995.

2. Hoogers, G., "The fueling problem: Fuel cell systems", *Fuel cell technology handbook*, CRC Press, pp. 114-136, 2002.

3. Wengenmayr R., Thomas B., *Renewable Energy: Sustainable Energy Concepts for the Energy Future,* John Wiley and Sons, 2nd edition, 2012.

4. Grove, W. R., "On a new voltaic combination", *Philosophical Magazine and Journal of Science*, Vol. 13, pp. 430-431, 1838.

5. Minh N.Q., Takahashi T., "Science and Technology of Ceramic Fuel Cells", *Elsevier*, 1995.

6. Singhal S. C., "Solid Oxide Fuel Cells: An Overview", *American Chemical Society, Div. Fuel Chem.*, Vol. 49 (2), pp. 478, 2004.

7. Demin, A., "Modified planar cell (MPC) and stack based on MPC", U.S. Patent No 8,409,763, 2013.

8. Kharton, V. V., *Solid state electrochemistry II: electrodes, interfaces and ceramic membranes*. John Wiley & Sons, 2012.

9. Huber, J. M., Lindstrom, J. D., Daggett, D. L., Friend, M. G., "Solid oxide fuel cell as auxiliary power source installation in transport aircraft." U.S. Patent 6,641,084, 2003.

10. Kharton, V. V., ed. *Solid state electrochemistry II: electrodes, interfaces and ceramic membranes*. John Wiley & Sons, 2012.

11. Laosiripojana, N., Wiyaratn, W., Kiatkittipong, W., Arpornwichanop, A., Soottitantawat, A. and Assabumrungrat, S., “Reviews on solid oxide fuel cell technology”, *Engineering Journal,* Vol. 13, pp. 65-84, 2009.

12. Vivet, N., Chupin, S., Estrade, E., Richard, A., Bonnamy, S., Rochais, D. and Bruneton, E., “Effect of Ni content in SOFC Ni-YSZ cermets: A three-dimensional study by FIB-SEM tomography”, *Journal of Power Sources*, Vol. 196, pp. 9989-9997, 2011.

13. Shishkin, M., and Ziegler, T., "Hydrogen oxidation at the Ni/yttria-stabilized zirconia interface: a study based on density functional theory." *The Journal of Physical Chemistry C,* Vol. 114, pp. 11209-11214, 2010.

14. Rossmeisl, J., and Bessler, W.G., "Trends in catalytic activity for SOFC anode materials.", *Solid State Ionics,* Vol. 178, pp. 1694-1700, 2008.

15. Hua, B., Zhang, W., Li, M., Wang, X., Chi, B., Pu, J., Li, J. (2014). “Improved microstructure and performance of Ni-based anode for intermediate temperature solid oxide fuel cells”, *Journal of Power Sources*, Vol. 247, pp. 170-177, 2014.

16. Kuhn, J., Kesler, O., “Carbon deposition thresholds on nickel-based solid oxide fuel cell anodes I. Fuel utilization”, *Journal of Power Sources*, Vol. 277, pp. 443-454, 2015.

17. Park, H., Li, X., Lai, S. Y., Chen, D., Blinn, K. S., Liu, M., Bottomley, L. A., “Electrostatic force microscopic characterization of early stage carbon deposition on nickel anodes in solid oxide fuel cells”, *Nano letters*, Vol. 15, 6047-6050, 2015.

18. Offer, G. J., Brandon, N. P., “The effect of current density and temperature on the degradation of nickel cermet electrodes by carbon monoxide in solid oxide fuel cells”, *Chemical Engineering Science*, Vol. 64, pp. 2291-2300, 2009.

19. Kuhn, J., Kesler, O., “Method for in situ carbon deposition measurement for solid oxide fuel cells”, *Journal of Power Sources*, Vol. 246, pp. 430-437, 2014.

20. Lu, M., *Materials for high-temperature fuel cells*, John Wiley & Sons, 2013.

21. Lashtabeg, A., Skinner, S. J., “Solid oxide fuel cells - A challenge for materials chemists”, *Journal of Materials Chemistry*, Vol. 16, pp. 3161-3170, 2006.

22. Berke, R. B., Walter, M. E., “Mechanical characterization of thin SOFC electrolytes with honeycomb support”, *Journal of Fuel Cell Science and Technology*, Vol. 10, p. 11001, 2013.

23. Zuo, C., Liu, M., Liu, M., “Solid oxide fuel cells”, *Sol-gel processing for conventional and alternative energy*, *Springer,* pp. 7-36, 2012.

24. Song, C., Zhang, J., “Electrocatalytic oxygen reduction reaction”, *PEM fuel cell electrocatalysts and catalyst layers,* Springer, pp. 89-134, 2008.

25. Navrotsky, A., “Energetics and crystal chemical systematics among ilmenite, lithium niobate, and perovskite structures”, *Chemistry of Materials*, Vol. 10, pp. 2787-2793, 1998.

26. Sun, C., Hui, R., Roller, J., “Cathode materials for solid oxide fuel cells: a review”, *Journal of Solid State Electrochemistry*, Vol 14, pp. 1125-1144, 2010.

27. Brett, D. J., Atkinson, A., Brandon, N. P., Skinner, S. J., “Intermediate temperature solid oxide fuel cells”, *Chemical Society Reviews*, Vol. 37, pp. 1568-1578, 2008.

28. Bragg, W. H., WL Bragg, B. A., “The reflection of X-rays by crystals”, *Proc. R. Soc. Lond. A*, Vol 88, pp. 428-438, 1913.

29. Briggs, D. "Handbook of X-ray and Ultraviolet Photoelectron Spectroscopy", London, 1977. *There is no corresponding record for this reference*.

30. Hadjarab, F., Erskine, J. L., "Image properties of the hemispherical analyzer applied to multichannel energy detection", *Journal of electron spectroscopy and related phenomena*, Vol. 36, pp. 227-243, 1985.

31. Princi, E., *Handbook of Polymers in Paper Conservation*, Smithers Rapra, 2011.

32. Lyman, C. E., Newbury, D. E., Goldstein, J., Williams, D. B., Romig Jr, A. D., Armstrong, J., Peters, K. R., *Scanning electron microscopy, X-ray microanalysis, and analytical electron microscopy: a laboratory workbook*, Springer Science & Business Media, 2012.

33. Kissinger, P., Heineman, W. R., *Laboratory Techniques in Electroanalytical Chemistry, revised and expanded*. CRC press, 1996.

34. Thomas, F. G., Henze, G., *Introduction to voltammetric analysis: theory and practice*. Csiro Publishing, 2001.

35. Bard, A. J., Stratmann, M., *Encyclopedia of electrochemistry: Index*. Wiley-VCh, 2007.

36. Malzbender, J., Steinbrech, R. W., Singheiser, L., "Determination of the interfacial fracture energies of cathodes and glass ceramic sealants in a planar solid-oxide fuel cell design". *Journal of materials research*, Vol. 18, pp. 929-934, 2003.

37. Ettler, M., Blaß, G., Menzler, N. H., "Characterisation of Ni–YSZ-Cermets with Respect to Redox Stability" *Fuel cells*, Vol. *7*, pp. 349-355, 2007.

38. Faes, A., Hessler-Wyser, A., Zryd, A., "A review of redox cycling of solid oxide fuel cells anode", *Membranes*, Vol 2, pp. 585-66, 2012.

39. Jiang, S. P., "A review of wet impregnation - an alternative method for the fabrication of high performance and nano-structured electrodes of solid oxide fuel cells", *Materials Science and Engineering: A*, Vol. 418, pp. 199-210, 2006.

40. Staffell, I., Brett, D. J., Brandon, N. P., Hawkes, A. D., "*Domestic microgeneration: renewable and distributed energy technologies, policies and economics*" Routledge, 2015.

41. Rossmeisl, J., Bessler, W. G., "Trends in catalytic activity for SOFC anode materials", *Solid State Ionics*, Vol. 178, pp. 1694-1700, 2008.

42. Shuguang, H., "XPS nondestructive depth analysis method and its application in cement based composite materials", *Cement and concrete research*, Vol 24, pp. 1509-1514, 1994.

43. Tan, B. J., Klabunde, K. J., Sherwood, P. M., "XPS studies of solvated metal atom dispersed (SMAD) catalysts. Evidence for layered cobalt-manganese particles on alumina and silica", *Journal of the American Chemical Society*, Vol. 113, pp. 855-861, 1991.

44. Weisentein, A. J., Childs, N., Amendola, R., Driscoll, D., Sofie, S. W., Gannon, P., Smith, R., "Processing and characterization of Sr2− xVMoO6− δ double perovskites", *Materials Chemistry and Physics*, Vol. 139, pp. 706-718, 2013.

45. Kasperkiewicz, J., Kovacich, J. A., Lichtman, D., "XPS studies of vanadium and vanadium oxides", *Journal of electron spectroscopy and related phenomena*, Vol. 32, pp. 123-132, 1983.

46. Cai, J., Gervasio, D. F., "The Nature of Surface Oxides on Corrosion-Resistant Nickel Alloy Covered by Alkaline Water", *Nanoscale research letters*, Vol 5, p. 613, 2010.

47. Orazem, M. E., Tribollet, B., *Electrochemical impedance spectroscopy*, John Wiley & Sons, Vol. 48, 2011.